Dalton Transactions

An international journal of inorganic chemistry

Accepted Manuscript

This article can be cited before page numbers have been issued, to do this please use: M. Hejda, L. Dostál, O. Mrózek, A. Růžika, A. Lyka, T. Mikysek, R. Jirásko and M. A. Samsonov, *Dalton Trans.*, 2026, DOI: 10.1039/D6DT01280A.

ROYAL SOCIETY OF CHEMISTRY

rsc.li/dalton

Journal Name ARTICLE

View Article Online
DOI: 10.1039/D6DT01280A

Boron-Targeted H-Atom Transfer Drives Disproportionation of 2,1-Benzazaborolyl Radical Anions Beyond Reversible Gomberg-Krause Dimerization

Received 00th January 20xx,
Accepted 00th January 20xx

DOI: 10.1039/x0xx00000x

Martin Hejda,*[a] Libor Dostál,[a] Ondřej Mrózek,[a] Aleš Růžička,[a] Antonín Lyčka,[b] Tomáš Mikysek,[c] Robert Jirásko,[c] and Maksim A. Samsonov[a]

This contribution provides a detailed mechanistic insight into a remarkably complex reaction of neutral 1-Ph-2-*tert*-butyl-1*H*-1,2-benzazaborole (**1**) with elemental potassium in THF, yielding the known 10π-aromatic 1*H*-2,1-benzazaborolyl (*2,1-Bab*$^-$) potassium salt (**2**), an isoelectronic species with indenyl potassium, along with a racemic mixture of a new potassium hydridoborate complex (**3**), formed together with **2** in ca. 1:1 molar ratio. Unlike derivatives of isoelectronic 1*H*-indene, which undergo various self-protonation processes under analogous conditions, for **1**, we propose a completely different and rather complex, non-linear tandem mechanism. Key species are four enantiomeric pairs of short-lived, dimeric, diamagnetic intermediates, denoted **α**, **β**, **ω₁** and **ω₂**, possessing structures related to Gomberg's dimer and Krause's adduct. Based on an exhaustive multinuclear NMR analysis of the reaction mixture, including experiments with *C3*-methylene deuterium-labelled starting compound **1-*d*$_n$** (n ∈ {0–2}) and the observation of a primary AKIE (k_H/k_D >> 1), as well as a detailed analysis of full scan mass spectra and observed ions in ultrahigh-resolution LDI-MS data of the resulting mixture of isotopologues of the final product **3-*d*$_n$** (n ∈ {0–4}), comprising multiple isotopomers, in combination with probabilistic calculations, electrochemical studies, and DFT calculations, we were able to reconstruct the full sequence of reaction steps and pathways. The presented results support the involvement of various H-atom transfer (HAT) processes within pairs of radical-anionic species **K$^+$1$^{\bullet-}$**, proceeding throught different transition states, and, most notably, reveal an extremely rare boron-targeted HAT. These findings provide a basis for developing synthetic routes to unconventional boron hydrides.

Introduction

The structural and electronic diversity of boron-containing species has expanded rapidly in recent decades, encompassing (anti)aromatic ring systems,[1-5] or cationic boron centres,[6] and, notably compounds in which boron acts as a spin carrier (Scheme 1A,D).[7-21] Particularly striking are advances in accessing highly unusual electronic states, including the formation of a boryl radical anion from a hexaaryldiboron(6) dianion[22] (Scheme 1A'), as well as the isolation of nucleophilic boryl anions[23-26] (Scheme 1B) and the long-sought nucleophilic boryl dianion[27-29] (Scheme 1C). These developments highlight the increasing accessibility of electron-rich and unconventional boron species, opening new directions in main-group reactivity. Further expansion of this landscape can be achieved by introducing additional heteroatoms into the boron framework. In this regard, substitution of a C=C unit by an isoelectronic, isosteric, and isolobal B(sp²)–N(sp²) bond represents the oldest but powerful and widely employed strategy for modulating electronic structure and reactivity.[30] This concept has been broadly implemented across diverse molecular platforms,[31-49] including stable boron-centred radical systems featuring B(sp²)–N(sp²) motifs (Scheme 1D).[8, 9, 50-56]

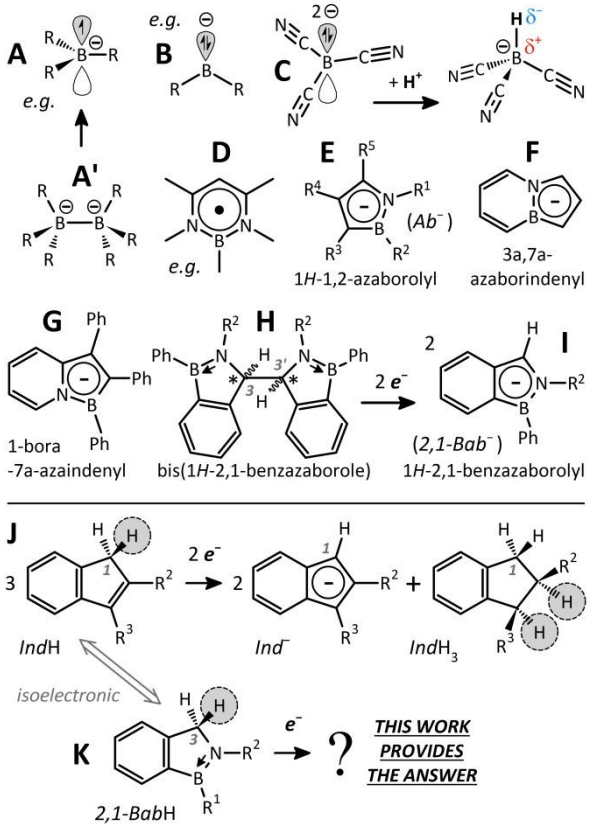

Scheme 1: Representative examples of the discussed classes of boron species (A – D) and *Cp*$^-$ and *Ind*$^-$ analogues containing a B(sp²)–N(sp²) bond (E – I). Summary of the electrochemical or alkali metal reduction of variously substituted *Ind*H derivatives reported in the literature,[57-64] illustrated here for 2,3-disubstituted derivatives (J), together with the questioned reactivity of an isoelectronic 1,2-disubstituted *2,1-Bab*H derivative (K).

[a] *Department of General and Inorganic Chemistry,* Faculty of Chemical Technology, *University of Pardubice, Studentská 573, CZ 532 10 Pardubice, Czech Republic. Email: martin.hejda@upce.cz*
[b] *Faculty of Science, University of Hradec Králové, Rokitanského 62, CZ 500 03, Hradec Králové 3, Czech Republic.*
[c] Department of Analytical Chemistry, Faculty of Chemical Technology, University of Pardubice, *Studentská 573, CZ 532 10 Pardubice, Czech Republic.*

Electronic Supplementary Information (ESI) available: [details of any supplementary information available should be included here]. See DOI: 10.1039/x0xx00000x

Besides these exotic species, a unique historical role is played by the 1,2-azaborolyl anion (*Ab*$^-$) (Scheme 1E), a five-membered C_3BN ring representing a 6π-aromatic analogue of the cyclopentadienyl anion (*Cp*$^-$). The chemistry of this system was pioneered by Schmid and co-workers in the 1980s,[65-68] while subsequent studies have focused primarily on transition- and rare-earth-metal complexes, particularly in the context of olefin polymerization[69-76] and asymmetric catalysis.[70, 77]

Beyond *Ab*$^-$, several positional isomers of 10π-aromatic B(sp^2)-N(sp^2) congeners of the 1*H*-indenyl anion (*Ind*$^-$) have emerged since the early 2000s, in some cases accompanied by their neutral *Ind*H-like conjugated C-H acid. However, their reactivity and coordination chemistry remain largely unexplored. Among these, the most extensively studied systems are the 3a,7a-azaborindenyl anion[78] (Scheme 1F) and 1-bora-7a-azaindenyl anion (Scheme 1G).[79] In addition, several neutral 1*H*-1,2-benzazaboroles have been reported,[80, 81] although the most prevalent B(sp^2)–N(sp^2) congener of *Ind*H is a 1*H*-2,1-benzazaborole (hereafter *2,1-Bab*H; Scheme 1K).[82-88] We have recently developed a convenient synthetic route to 1,2,3-trisubstituted *2,1-Bab*H derivatives,[39, 89] and subsequently reported the first examples of 1,2-disubstituted *2,1-Bab*$^-$ anions (Scheme 1I) as alkali metal salts M$^+$*2,1-Bab*$^-$ (M = Li, Na, K) obtained *via* mesolytic C(sp^3)–C(sp^3) bond cleavage in (3,3')-bis(*2,1-Bab*H) dimers (Scheme 1H) upon alkali metal reduction.[90, 91]

Given the unusual reactivity of these dimeric precursors[91] and the lack of systematic mechanistic studies on B(sp^2)–N(sp^2) congeners of 1*H*-indene, we set out to investigate the reaction of a monomeric 1,2-disubstituted *2,1-Bab*H derivative with alkali metals (Scheme 1K). Owing to its isoelectronic relationship with *Ind*H, a key question was whether its reactivity would follow the well-established pathways described for substituted *Cp*H[92] and *Ind*H derivatives[57-64] under electrochemical or alkali metal reduction, illustrated here for 2,3-disubstituted-*Ind*H derivatives (Scheme 1J). In these systems, single electron transfer (SET) to *Ind*H generates radical anion (*Ind*H$^{\bullet-}$), which in aprotic media undergoes rapid "father-son" self-protonation[93] from (*C1*)H-acidic methine group of the parent substrate itself, ultimately yielding the indenyl anion (*Ind*$^-$) and saturated indane (*Ind*H$_3$) in *syn*-configuration around the *C2*(sp^3)–*C3*(sp^3) bond (Scheme 1J). In the absence of a suitable proton donor, further reduction of *Ind*$^-$ or disproportionation of the two *Ind*H$^{\bullet-}$ leads to dianionic species (*Ind*H^{2-}), which act as Brønsted bases and reductants and are subsequently quenched *via* alternative protonation pathways,[93 64] affording the same two final products or indane *Ind*H$_3$ with *anti*- configuration around the *C2*(sp^3)–*C3*(sp^3) bond. Overall, this sequence can be viewed as a Birch-type reduction of the C=C bond.

In contrast, analogous reduction of the B(sp^2)–N(sp^2) bond in the studied case of 1,2-disubstituted *2,1-Bab*H (Scheme 1K) is far from trivial. Formation of a B–H bond within R^{1}HB(sp^3)←N(sp^2)HR^2 fragment (Scheme 2; top) would require a protonation of an over-reduced nucleophilic boryl dianion (*2,1-Bab*H^{2-}) with a lone electron pair (LEP) at boron, an extremely rare and electronically demanding species (Scheme 1C).[28, 29] Considering this, a more plausible pathway appeared to be simple deprotonation at the *C3*-methylene position, leading to formation of alkali metal salt M$^+$2,1-*Bab*$^-$ with concomitant H_2 evolution (Scheme 2; middle), analogous to the behaviour of unsubstituted *Ind*H.[63]

Unexpectedly, the observed reactivity deviates markedly from these scenarios. Herein, we report a previously unrecognized, non-linear tandem mechanism involving multiple thermodynamically metastable intermediates and featuring an exceptionally rare boron-targeted H-atom transfer. This study uncovers an unprecedented mode of reactivity at the interface of boron and organic radical chemistry.

Results and discussion

Initial reduction of 1*H*-2,1-Benzazaborole (1) with potassium: Defining the scope of the study

To address the above question, a *ca.* 0.3 mol dm^{-3} solution of colourless 1-phenyl-2-*tert*-butyl-1*H*-2,1-benzazaborole (**1**; see the SI for synthesis) in THF-d_8 was treated with a potassium mirror (1:1 molar ratio) at room temperature under rigorously anaerobic and anhydrous conditions. Strikingly, no gas evolution (anticipated as H_2) was observed; instead, the reaction immediately produced a deep red solution (time (t) = 0). As the potassium metal was gradually consumed from the walls of the Schlenk tube (t = 45 min), the colour intensity increased. However, by the time of NMR analysis (t = 60 min), the solution had shifted to a blood-red colour. While NMR spectroscopy confirmed the formation of the expected blood red 2,1-*Bab*$^-$ potassium salt[90, 91] (**2**), it simultaneously revealed the formation of a second product. Unexpectedly, a racemic mixture of new potassium hydridoborate complex (**3**) was generated alongside **2** in approx. 1:1 molar ratio (*vide infra*) (Scheme 2), directly contradicting the anticipated reaction outcome and pointing to a fundamentally different reaction pathway.

View Article Online
DOI: 10.1039/D6DT01280A

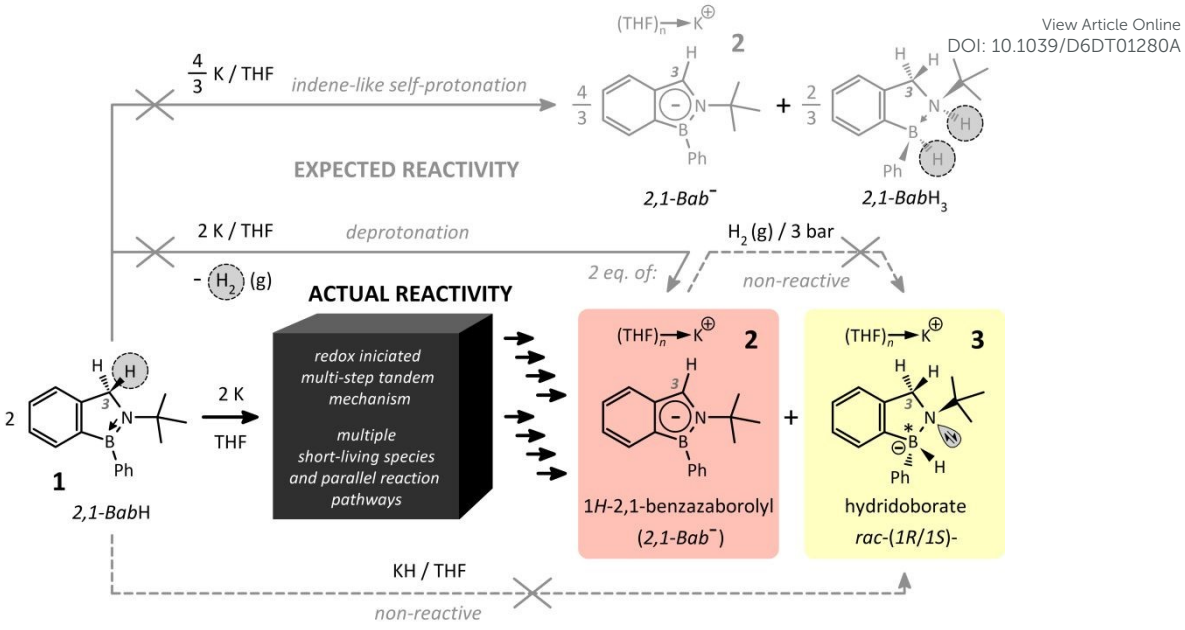

Scheme 2: Overview of the unexpected reaction outcome between **1** and potassium in THF, highlighting the final products and key observations, including the lack of reactivity of **1** toward hydride sources and of **2** toward H_2 (dashed arrows), thereby pointing to an alternative mechanism for the formation of **3**. Only the 1S enantiomer of **3** is shown for clarity.

Although monohydrogenated **3** was formed instead of the expected dihydrogenated *2,1-Bab*H3 (Scheme 2, top) and the products were obtained in a 1:1 rather than 2:1 molar ratio, the N(LEP)–B^- fragment present in **3** remains isoelectronic and isolobal with the H–C2(sp^3)–C3(sp^3)–H fragment in indane (*Ind*H_3) (Figure 1). Consequently, the fundamental mismatch in polarity between the B(δ^+)–H(δ^-) bond in **3** and the C3(δ^-)–H(δ^+) bond in *Ind*H_3 persists. This observation points to a mechanistic pathway for the reaction of **1** with potassium that differs fundamentally from that established for *Ind*H.

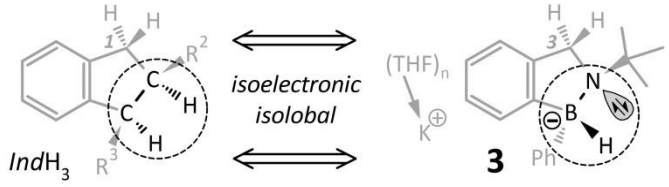

Figure 1: At first glance, the H–*C2*(sp^3)–*C3*(sp^3)–H and N(LEP)–B^- fragments appear analogous, suggesting a similar formation mechanism.

A direct comparison of **1** and **3** suggests that formation of **3** from **1** would formally require one equivalent of potassium hydride. However, compound **1** proved inert toward hydride sources (Scheme 2, see the SI for details). Conversely, formation of **3** from **2** would formally require one equivalent of dihydrogen. Thus, if H_2 were generated during the reaction alongside **2**, it could, in principle, react *in situ* to give **3**. Yet, no reactivity of **2** toward H_2 was observed, even at 3 bar (Scheme 2).

However, a striking feature of the reaction of **1** with potassium lies in the transient formation of multiple intermediates of unknown structure (*vide infra*), despite **2** and **3** being the final products. These species rapidly diminish over time and are fully converted into **2** and **3** within 90 min. Their transient nature and clean conversion into **2** and **3** strongly indicate a complex and unprecedented reaction mechanism (Scheme 2, "*black box*").

Identification and characterisation of the final products 2 and 3

The identity of compound **2**, a known potassium salt of the aromatic *2,1-Bab*$^-$ anion, was confirmed by an excellent match of the ^{1}H, ^{11}B, ^{13}C, and ^{15}N NMR data with those previously reported earlier[90, 91] for isolated **2** prepared according to Scheme 1I. Notably, several signals render the NMR spectra of the *2,1-Bab*$^-$ anion in THF-d_8 highly characteristic (*cf.* C and D in Figure 4).

The structure of the new potassium hydridoborate complex **3** formed alongside **2** was elucidated using 1D and 2D ^{1}H, ^{11}B, ^{13}C, and ^{15}N NMR correlation and exchange experiments (see SI for full NMR assignment). A cross-peak observed in the ^{1}H-^{15}N HMBC spectrum at $\delta(^{15}N)$ = −332.4 ppm (*cf.* −235.2 and −208.7 ppm for **1** and **2**, respectively; referenced to CH_3NO_2, $\delta(^{15}N)$ = 0.0 ppm; Figures S5 and S18) falls within the range characteristic of *B*-bound N(sp^3) atoms bearing a LEP.[91] Together, the B and N atom formally constitute two stereogenic centres in the anionic part of **3** (*vide infra*). In contrast to **1**, where the (C3)H_2 methylene bridge appears as a singlet in the ^{1}H NMR spectrum, it becomes diastereotopic in **3**, giving rise to an AX spin system at 4.12 and 4.44 ppm with ^2J (^{1}H, ^{1}H) = 13.0 Hz. The hydridic B–*H* proton resonates as a broad multiplet at 3.32 ppm, reflecting coupling to both ^{11}B and ^{10}B nuclei. Importantly, the observed $^1J(^{11}B,^1H)$ coupling constant of 84.3 Hz corresponds to a sharp doublet in the ^{11}B NMR spectrum at −4.8 ppm (Figure 4C), consistent with values reported for methylborate complexes of the same *2,1-Bab* framework.[91]

Following work-up (see SI), complex **3** was isolated in high yield (80%) by fractional crystallization of its 18-crown-6 adduct and fully characterized. The solid-state structure of [**3**·(18-crown-6)·$(THF)_4$] was determined by single-crystal X-ray diffraction (Figure 2). The potassium cation is coordinated by the 18-crown-6 ether ligand in the equatorial plane and by two THF molecules in axial positions, resulting in effective spatial separation from the hydridoborate anion. However, a NOE cross-peak between the *t*Bu protons and the -CH_2-CH_2- units of 18-crown-6 in the 2D ^{1}H-^{1}H NOESY spectrum (Figure S23) indicates that the cation remains in close proximity to the anion in the solution. Accordingly, [**3**·(18-crown-6)·$(THF)_4$] forms contact ion pairs in THF, consistent with the solid-state structure (Figure 2), where the shortest H···H contact between the ionic components is 2.43 Å.

Despite crystallographic disorder arising from the positioning of B1, H1, N1, and C8 atoms (*tert*-butyl group) on special positions in the monoclinic space group C_c, the structure unambiguously reveals a racemic mixture of (1*R*,2*S*) and (1*S*,2*R*) enantiomers of the anionic fragment, with tetrahedral B1 and N1 centres. The B1–H1 bond length of 1.09(8) Å [Σ_{rcov}(B-H) = 1.17 Å[94]] is comparable to that in $K[BH_4]$,[95] and the B–H stretching frequency (2324 cm^{-1}) is consistent with values reported for borohydride species.[96]

Both boron and nitrogen atoms are formally sp^3 hybridized, and the B-N bond therefore exhibits single-bond character, in contrast to compound **2**.[90] This is reflected in the B1–N1 bond length of 1.571(13) Å [Σ_{rcov}(N-B) = 1.56 Å[94]]. Consequently, the C_3BN ring in **3** lacks π-electron delocalization, consistent with its colourless appearance, in contrast to the intensively coloured aromatic anion **2**. In both enantiomers, the *B*-bound phenyl group and the *N*-bound *t*Bu substituent adopt an *anti*-configuration. Although the presence of a stereogenic boron centre adjacent to a pyramidal nitrogen atom allows, in principle, for diastereomer formation, only a single set of NMR signals is observed (both in the isolated complex and in the reaction mixture), indicating rapid inversion at nitrogen on the NMR timescale.

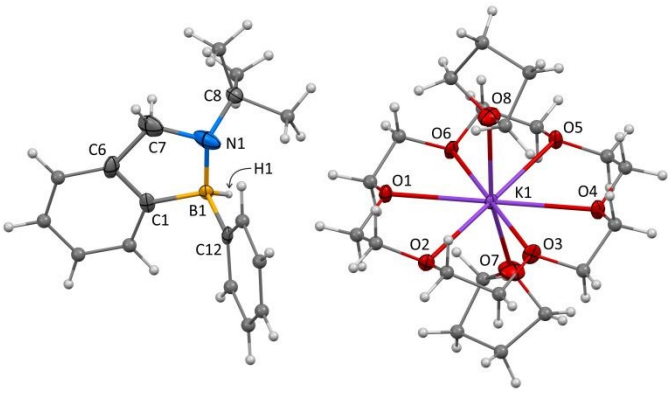

Figure 2: Molecular structure of 1*S*-enantiomer of *rac*-(1*R*/1*S*)-[**3**·(18-crown-6)·$(THF)_4$] showing 40% probability thermal ellipsoids. In the solid state at 150 K, the nitrogen atom in the position 2 is pyramidalized, thus appearing as *anti*- configuration, i.e. (1*S*,2*R*)-, of the *rac*-(1*S*,2*R*)/(1*R*,2*S*)- configurations. Two co-crystalized molecules of THF are omitted for clarity. Selected bond lengths [Å], bonding angles [deg] and torsion angle [deg]: B1-N1 1.571(13), N1-C7 1.550(19), C7-C6 1.55(2), C6-C1 1.372(13), C1-B1 1.607(11), C1-B1-N1 106.5(6), B1-N1-C7 94.7(9), N1-C7-C6 121.8(13), C6-C1-B1 118.0(8), C1-B1-N1 106.5(6), C12-B1-N1-C8 119.6(9).

Mechanistic insight into the early stages of the reaction

Upon addition of a colourless solution of **1** in THF-d_8 to a potassium mirror at −50 °C in 1:1 molar ratio, the reaction rate was sufficiently reduced to allow observation of three distinct colour changes during potassium consumption, followed by a less pronounced fourth transition thereafter. The first change occurred immediately (t = 0), as a deep red solution formed throughout the reaction mixture (A and A' in Figure 3).

The subsequent two changes of colour were observable only in the absence of stirring. When the potassium mirror was not fully submerged, a thin dark blue layer formed on its surface (Figure 3B), likely corresponding to a radical-anionic species $\mathbf{K^+1^{\bullet-}}$ generated by reduction of **1** (*vide infra*). This transient blue layer disappeared upon contact with the bulk solution, consistent with rapid reaction either with itself or with unreacted **1** still present in the mixture.

After a few seconds, a dark green species (λ_{max} abs = 636 nm; see Figure S25) emerged at the interface with the submerged potassium (Figure 3C) and diffused into the deep red solution. This species was observable only while unreacted potassium remained and rapidly vanished upon diffusion, again suggesting reaction with residual **1**. Its behaviour is consistent with formation *via* over-reduction (*vide infra*).

Once the potassium was fully consumed (ca. 45 min under sonication at 0 °C), and the reaction mixture was allowed to warm to room temperature, a final, fourth colour change gradually occurred.[97] The deep red solution slowly faded over 90 min, yielding a blood red mixture containing exclusively **2** and *rac*-(1*R*/1*S*)-**3** (Figure 3D and D'), as confirmed by multinuclear NMR spectroscopy (Figure 4C). Notably, this final mixture showed no further reactivity toward additional potassium.[98]

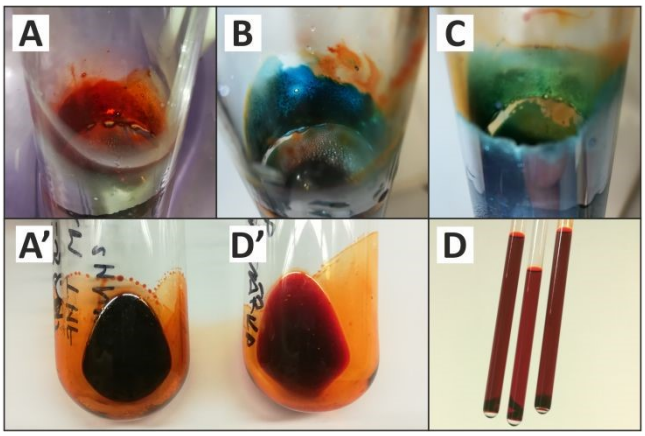

Figure 3: Observed colour changes during consumption of potassium metal (mirror) within a single batch (A – C) and in flame-sealed NMR tubes from various batches containing the final blood red solution of products **2** and **3** (D), formed over time from the initial deep red solution (A'). *Notes:* Images A' and D' correspond to different batches at comparable concentrations but at different stages of the reaction: the deep red solution immediately after complete consumption of potassium (A') and the final blood red solution containing **2** and **3** (D'). Image D also shows a small amount of dark solid residue at the bottom of the NMR tubes precipitated over time.

View Article Online
DOI: 10.1039/D6DT01280A

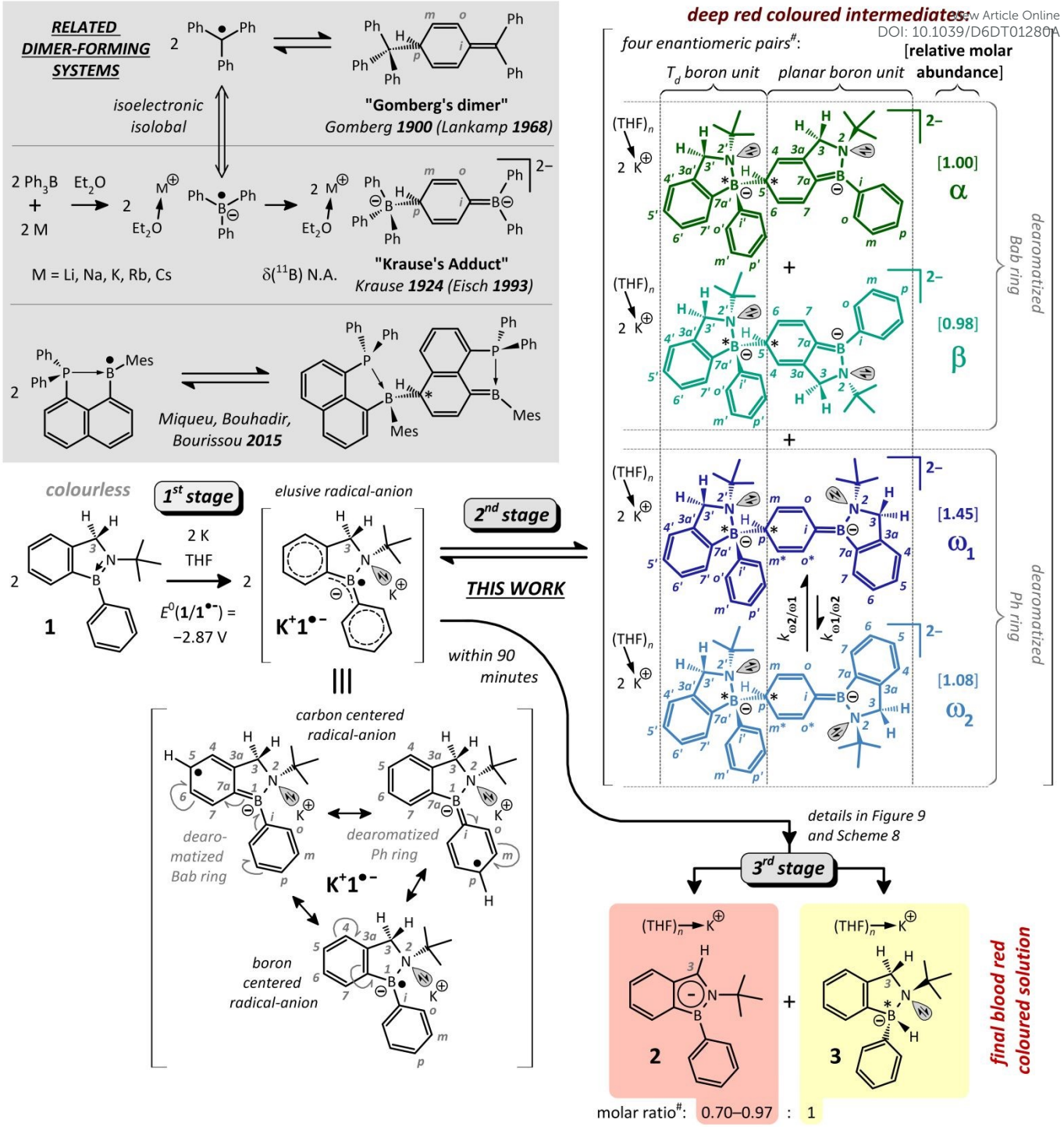

Scheme 3: Gomberg-/Krause-type dimers relevant to this study and their transient formation during the potassium-mediated reduction of **1**, ultimately yielding a mixture of **2** and **3**. In the case of $K^+1^{\bullet-}$, only the dominant resonance forms are shown (for plots of the SOMO and the spin-density map, see Figure 6; for a list of spin densities, see Figure S67). Redox potential is referenced to SCE. (#) Each of the intermediates **α**, **β**, ω_1 and ω_2 is formed as a racemate; thus, a total of eight stereoisomeric intermediates are present. For clarity, only one enantiomer is shown in each case. (#) - Varies from batch to batch. The origin of this phenomenon is discussed further below.

To characterize the species present in the deep red solution (Figure 3A and A'), a sample from the low-temperature experiment was quickly analysed by NMR spectroscopy at room temperature immediately after complete consumption of potassium. Owing to the intrinsic instability and short lifetime (ca. 1 h) of these intermediates at room temperature, the NMR investigation was limited to basic 1D experiments. Nevertheless, the obtained spectra proved to be remarkably complex. For instance, the ^{1}H NMR spectrum (Figure 4B) displayed several dozen sharp yet heavily overlapping signals spanning the entire region from aliphatic to aromatic chemical shifts (see Figure S8 for the full spectrum).

View Article Online
DOI: 10.1039/D6DT01280A

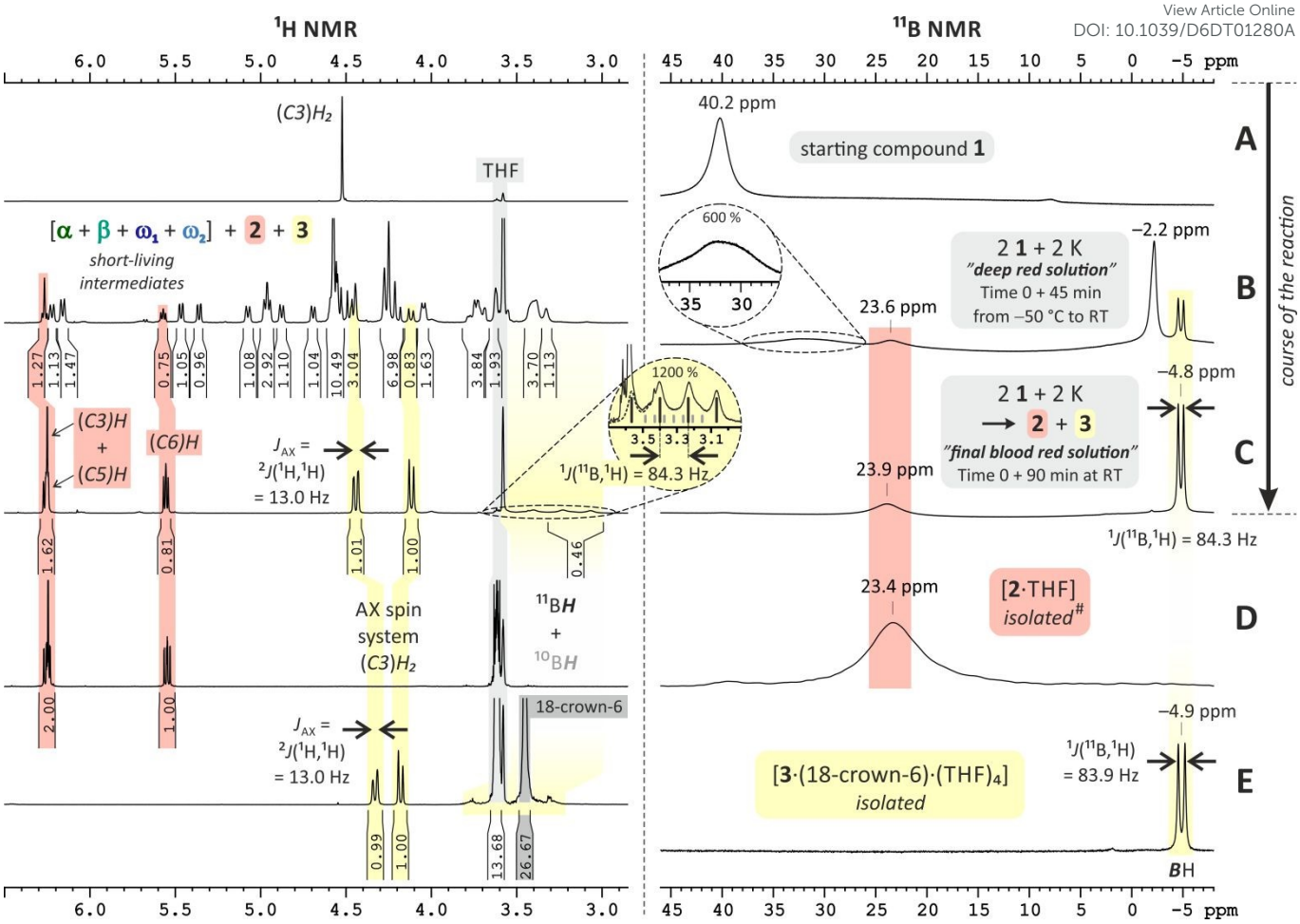

Figure 4: Expanded view of stacked ^{1}H NMR spectra (500.20 or 400.13 MHz, THF-d_8, 21 °C) and full ^{11}B NMR spectra (160.48 MHz, THF-d_8, 21 °C) recorded at various stages of the reaction between compound **1** and potassium metal in THF-d_8 (A – C). Spectrum (B) was acquired at 21 °C immediately after sample preparation. Data marked with # were previously reported.[90, 91] Full spectra are provided in SI.

In addition to these unidentified signals, minor resonances corresponding to the final products **2** and **3** were detected. Notably, these products were consistently present in an approximately 1:1 molar ratio, irrespective of the reaction progress (as defined by time). In contrast, no signals attributable to the starting material **1** were observed in any of the ^{1}H, ^{11}B, or ^{13}C NMR spectra of the deep red solution (*cf.* ^{11}B NMR spectra A and B in Figure 4).

Particularly notable was the crowded region of the ^{1}H NMR spectrum between 3.0 and 6.3 ppm, which contained dozens of unresolved, doublet-like resonances (Figure 4B). Based on their non-equivalent relative intensities (1:0.98:1.45:1.08),[99] we proposed that these signals arise from at least four distinct spin systems, corresponding to a minimum of four structurally related species. At that stage of the research, we tentatively assigned these species, denoted **α**, **β**, **ω$_1$** and **ω$_2$**, as products of dimerization of a radical anion **K$^+$1$^{\bullet-}$** formed *via* reduction of **1** by potassium. We supposed that these species may adopt structures analogous to the classical Krause's adduct, the dianionic dimer $[Ph_3B\text{-}C_6H_5\text{=}BPh_2]^{2-}$ (Scheme 3), reported nearly a century ago.[8, 100-102] This dimer is formed *via* Gomberg-type coupling of the triphenylboryl radical anion, reflecting the isoelectronic relationship between $Ph_3B^{\bullet-}$ and the neutral trityl radical $Ph_3C^{\bullet}$, which forms the well-known Gomberg's dimer.[8, 103-107] In the context of boron chemistry, a related dimerization process has more recently been described for an intramolecularly *P*-coordinated neutral boryl radical, which undergoes reversible Gomberg-like dimerization in solution (Scheme 3).[108, 109]

The plausibility of radical-anion dimerization in the reaction of **1** with potassium, leading to intermediates **α**, **β**, **ω$_1$** and **ω$_2$**, was supported by several observations. Although the ^{13}C{^{1}H} APT NMR spectrum of the deep red solution contained more than one hundred signals (Figures S10-S12), eight resonances (in addition to those of **2** and **3**) corresponding to *t*Bu and methylene (C3)H$_2$ groups could be readily identified. These signals could be grouped into two sets with slightly different chemical shifts, giving rise to four signals for each substituent.

Furthermore, despite the overall complexity of the ^{11}B NMR spectra (Figure 4B), two distinct types of signals were discernible in markedly different spectral regions. One appeared as an intense, sharp singlet at –2.2 ppm, while the other consisted of a set of overlapping broad signals in the

range from 30 to 34 ppm. These regions are characteristic of tetrahedral (T_d) and trigonal planar (TP) boron centres coordinated to nitrogen,[65] respectively. This observation suggests that at least some (if not all) of the intermediates **α**, **β**, **ω₁** and **ω₂** contain both T_d- and TP-coordinated boron atoms within their structure, analogous to the Krause's dimer (Scheme 3).

Importantly, all four intermediates retain the methylene (*C3*)H_2 moiety, as evidenced by the $^{13}C\{^1H\}$ APT NMR spectra. Despite these insights, experimental structure determination remained highly challenging due to the spectral complexity and the inherent nature of these species, namely their short lifetimes and extreme sensitivity to trace amounts of air and moisture. Nevertheless, deuterium labelling ultimately enabled their elucidation (*vide infra*).

Subsequent reactions after initial reduction

The reaction sequence is initiated by a single-electron transfer (SET) from potassium to neutral compound **1**, affording the radical-anionic species **K⁺1•⁻**. In contrast to the radical anions of 2,3-disubstituted 1*H*-indenes,[77-82, 104] this species undergoes rapid dimerization to yield dianionic dimers with two potassium counter-cations, namely **α**, **β**, **ω₁** and **ω₂**. Notably, this dimerization is sufficiently fast that lowering the reaction temperature to −50 °C does not significantly affect the rate of formation of the deep red dimers in solution, but only slows their subsequent transformation into the final products **2** and **3**.

Importantly, multiple experiments demonstrated that the deep red solution is EPR silent,[110] while providing well-resolved NMR spectra (Figure 4B), indicating that all four dimers **α**, **β**, **ω₁** and **ω₂**, are most likely closed-shell singlet species. These observations initially suggested that reverse monomerization of the dimers is not thermodynamically favoured under the given conditions; however, EXSY NMR experiments and DFT calculations reveal the opposite behaviour (*vide infra*).

In addition to the initial SET between **1** and potassium, the pronounced colour changes observed during the early stages of the reaction suggested the involvement of further redox processes. Surprisingly, cyclic voltammetry revealed only a single cathodic redox event within the accessible potential window (down to −3.2 V; Figure 5), corresponding to the reduction of **1** to the transient radical anion **1•⁻**. This process, with E^0(**1**/**1•⁻**) = −2.87 V *vs.* SCE, was quasi-reversible only at scan rate of 20 V s^{-1} and became fully irreversible at lower scan rates. Such behaviour is consistent with rapid consumption of **1•⁻** *via* dimerization to **α**, **β**, **ω₁** and **ω₂**. Given the highly negative reduction potential, it is not surprising that attempts to reduce **1** using potassium amalgam were unsuccessful.[111,112]

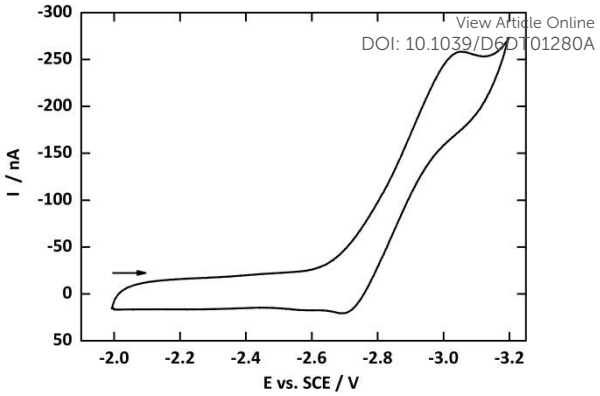

Figure 5: Cyclic voltammogram of **1** recorded under rigorously anaerobic and anhydrous conditions in vacuum-transferred THF at 21 °C (*vs.* SCE). A carbon fibre microelectrode (BASi MF-2007, 11 µm) was used as the working electrode, with 0.1 M nBu$_4$N$^+$PF$_6^-$ as the supporting electrolyte. Scan rate 20 V s^{-1}. The horizontal arrow indicates the direction of the forward potential sweep.

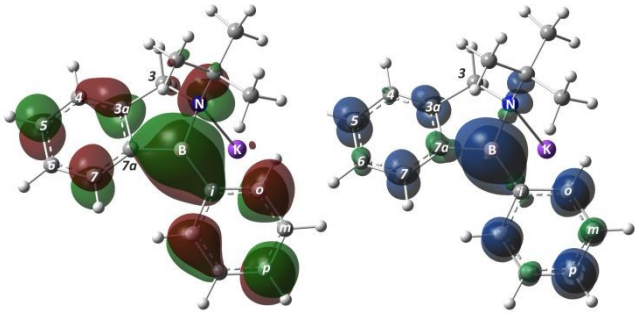

Figure 6: Plots of the SOMO (left) and the Mülliken spin-density map (right) of **K⁺1•⁻** calculated at the M062X/D3/def2-TZVP (PCM, THF) level of theory.

The DFT-optimised structure of **K⁺1•⁻** (M062X/D3/def2-TZVP, PCM (THF)) exhibits an essentially planar geometry at the boron centre (∑< 358.2°, see SI for atomic coordinates), consistent with the planar geometry of the kinetically stabilized trimesitylborane radical anion ($Mes_3B^{\bullet-}$), which does not undergo Gomberg- (or Krause-) type dimerization.[113]

In contrast to $Mes_3B^{\bullet-}$, where the C–B bonds are elongated by ca. 0.02 Å relative to neutral Mes_3B, the *C7a*–B bond length in **K⁺1•⁻** remains essentially unchanged, while the (*i*-C)–B bond is shortened by approximately 0.04 Å. This behaviour can be attributed to delocalisation of spin density (*vide infra*) through *p* orbitals, which induces co-planarization of the *B*-phenyl group with the *2,1-Bab*H ring upon reduction of **1**. In the neutral precursor, these ring systems are oriented nearly perpendicular to each other.

Analysis of the bonding pattern in **K⁺1•⁻**, including the alternation of C–C and C=C bonds, indicates that both the *B*-bound phenyl group and the C_6 ring of the *2,1-Bab*H core lose the aromatic character present in **1**. The most pronounced structural change relative to **1** is, however, the complete loss of double-bond character in the B–N bond. The nitrogen atom adopts a formal sp^3 hybridization and coordinates to the potassium cation, resulting in elongation of the B–N bond from 1.409 Å in **1** to 1.530 Å in **K⁺1•⁻**.

Calculated Mülliken/NBO spin density distributions (Figure 6) reveal that the unpaired electron in **K⁺1•⁻** is extensively delocalized, with the largest contributions located on the

boron atom (0.429/0.466) and on several carbon centres, including *p*-Ph (0.233/0.183), *o*-Ph (0.209/0.143), *o*'-Ph (0.163/0.108), *C5* (0.123/0.096), and *C7* (0.135/0.090), while the nitrogen atom carries negligible spin density (−0.034/0.009). These results identify the most probable sites for the proposed dimerization (Scheme 3 and *vide infra*).

As noted above, **K⁺1•⁻** is too short-lived to be directly observed in solution. Nevertheless, the pronounced colour changes observed during the initial stages of the redox process (Figure 3B) may reflect its transient formation. In particular, the thin, dark blue layer temporarily formed on the potassium mirror may correspond to this elusive species. To support this hypothesis, time-dependent DFT calculations were performed (see Section 5.1 in SI).

While the dark blue colour is most likely associated with **K⁺1•⁻**, the dark green colour (Figure 3C) is tentatively attributed to the formation of over-reduced species derived from the deep red dimers **α**, **β**, **ω₁** and **ω₂** upon further reduction by potassium metal (details in SI in Sections 2.6-2.8). Notably, regardless of whether formation of the dark green species was observed across different batches, the final outcome of the reaction remained unchanged, consistently yielding compounds **2** and **3** in an approximately 1:1 molar ratio.

Deuteration experiments

Given the limited mechanistic insight at this stage, we formulated three key questions that needed to be addressed: (i) what are the structures of the dimers **α**, **β**, **ω₁** and **ω₂**?; (ii) how are these intermediates converted into the final products **2** and **3**?; and (iii) what is the origin of the hydridic B–H hydrogen in **3**? The working hypothesis was that this hydrogen most likely originates from the (*C3*)H_2 methylene unit of **1**. However, alternative sources, such as the solvent or other C–H fragments of **1**, as well as subsequent hydrogen migration processes, could not be excluded.

To address the latter question, a strategy based on *C3*-deuterium-labelled **1** was devised. Using a total synthetic approach, an isotopic mixture comprising 93.7% *C3*-di-deuterated **1-*d*₂**, 5.9% *C3*-mono-deuterated **1-*d***, and 0.4% non-deuterated **1** (based on NMR analysis) was obtained, consistent with the isotopic composition of the starting materials (Scheme 4; see Sections 2.9–2.11 in the SI for details).

With *C3*-deuterium-labelled **1** in hand, all key mechanistic questions outlined above could, in principle, be addressed. Most importantly, reduction of the isotopologue mixture **1-*d*ₙ** (n ∈ {0, 1, 2}) with one equivalent of potassium in THF-d_8 afforded, despite the differing isotopic compositions, the same reaction outcome as observed for non-deuterated **1**, namely the formation of isotopologues of **2** and **3**. The consequences of deuterium incorporation are clearly reflected in the NMR spectra; the corresponding discussion on this matter can be found in Section 2.12 of the SI.

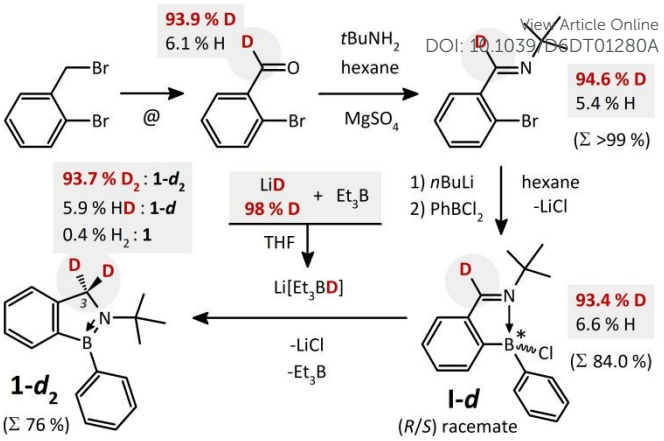

Scheme 4: Total synthesis of *C3*-di-deuterated 1*H*-2,1-benzaborole **1-*d*₂**. Deuterium enrichment was determined by ^{1}H NMR integration. Reagents and conditions: (@) synthesis according to ref. 114 (i) 4-methylpyridine, K_3PO_4, DMSO, D_2O (99.9% D); (ii) *N,N*-dimethyl-4-nitrosoaniline. Isolated yield is given in parentheses.

For the deuterium-labelled product **2-*d*ₙ**, containing the aromatic 2,1-*Bab*⁻ anion, ~99.6% of the material was *C3*-deuterated, while a minor fraction of non-deuterated **2** (~0.4%) was inevitably formed due to the presence of **1-*d*** (5.9%) and **1** (0.4 %) in the starting mixture. In addition to the expected mono-*C3*-deuterated isotopologue **2-*d***, which predominated (~81% and ~85% for batches A and B, respectively), a significant fraction corresponded to the di-deuterated isotopologue **2-*d*₂** (~19% and ~15% for batches A and B, respectively), in which deuterium is incorporated not only at the *C3*- position but also at *para*-phenyl carbon (*p*-Ph-C).

These species were further classified using the "**_*X*_*X***" notation (***X*** = H/D; Figure 7), denoting their relevant isotopomers, i.e. **2-*d*** as **_*D*_*H*** and **2-*d*₂** as **_*D*_*D***. The partial incorporation of deuterium at the unexpected *p*-Ph-C position in **2-*d*ₙ** (n ∈ {0, 1, 2}) (where **2-*d*₁ ≡ 2-*d***, while **2-*d*₀ ≡ 2**) represents a key mechanistic insight (*vide infra*). The predominance of **_*D*_*X*** isotopomers (i.e. both **2-*d*** and **2-*d*₂**) over the non-deuterated isotopologue **2** (**_*H*_*H***) is evident from the absence of the (*C3*)*H* singlet at 6.25 ppm in the ^{1}H NMR spectra (Figure S36D,E at page S35; batches A and B), and corroborated by the presence of a broad (*C3*)*D* broad signal at 6.28 ppm in the ^{2}H NMR spectrum (reaction performed and recorded separately in non-deuterated THF; batch C; Figure S36F at page S35). In the ^{13}C{^{1}H} NMR spectrum, the (*C3*)*D* group gives rise to a triplet at 96.4 ppm ($^1J(^{13}C,^2H)$ = 26.5 Hz; Figure S52).[115] Deuteration incorporation at the *p*-Ph position in the **_*D*_*D*** isotopomer of the **2-*d*₂** isotopologue is reflected in a reduced intensity of the corresponding (*p*-Ph)*H* triplet of triplet at 6.98 ppm in the ^{1}H NMR spectrum (Figure S36D,E at page S35; batches A and B), while the corresponding ^{2}H signal of the (*p*-Ph)*D* deuteron is broad and of low intensity (Figure S36F at page S35; batch C).

The situation is even more complex for the second product, the deuterium-labelled potassium borate **3-*d*ₙ**. The major isotopologues are the *C3*-di-deuterated hydridoborate **3-*d*₂** (two deuterium atoms in total) and the deuteridoborate **3-*d*₃** (three deuterium atoms in total), while smaller amounts

of a full series of isotopologues **3-d_n** (n ∈ {0, 1, 2, 3, 4}) are also observed (with **3-d_1** ≡ **3-*d*** and **3-d_0** ≡ **3**; see Table 1). Notably, the presence of a relatively abundant tetra-deuterated isotopologue **3-d_4** (9.7% in batch B based on LDI-MS analysis) was unexpected and pointed to a more complex mechanistic scenario.

Instead of three anticipated sites of deuterium incorporation in **3-d_n** (*C3* and boron), four distinct positions were identified, with the additional site corresponding to the *p*-Ph-C position. Detailed analysis of ultrahigh-resolution LDI-MS data, supported by NMR studies of isolated [**3-d_n**·(18-crown-6)·$(THF)_4$]) crystals (see SI, Sections 3.3–3.8), revealed that multiple isotopomers can contribute to a given isotopologue **3-d_n** (summarized in Table 1). For example, the 36.7% fraction of **3-d_2** consists predominantly of two isotopomers, ***HDDH*** (33.0%) and ***DHDH*** (3.7%), while the 46.1% fraction of **3-d_3** is mainly composed of ***DDDH*** (38.9%) and ***HDDD*** (7.2%), using the "***XXXX***" notation (***X*** = H/D; Figure 7).

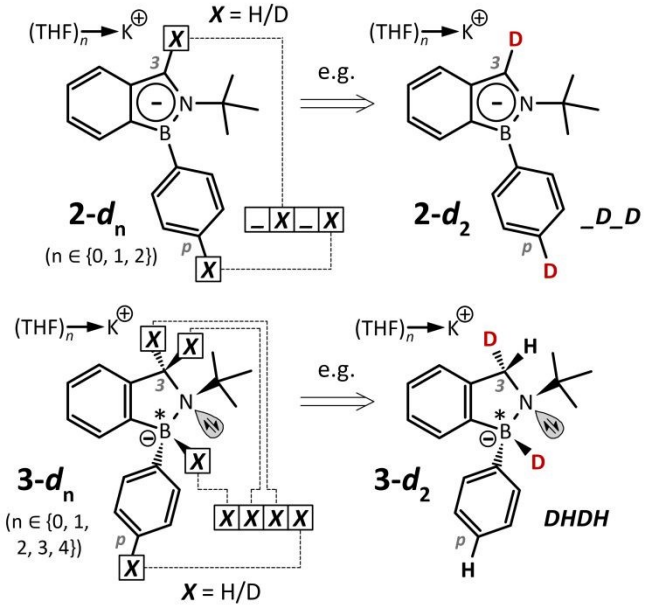

Figure 7: Definition of the "***_X_X***" and "***XXXX***" notation (***X*** = D/H) used to describe individual isotopomers of the isotopologues **2-d_n** (n ∈ {0–2}) and **3-d_n** (n ∈ {0–4}), respectively. The "***_X_X***" notation refers to substitution at the *C3*-methylene carbon and *p*-Ph carbon positions, whereas "***XXXX***" notation corresponds to substitution at the boron, *C3*-methylene, and *p*-Ph carbon positions. For simplicity, diastereotopic *C3*-methylene H/D atoms in ***XHDX*** and ***XDHX*** for **3-d_n** are not distinguished (i.e. ***XHDX*** ≡ ***XDHX***).

Although the same batch of starting material **1-d_n** was used, slight variations in the molar ratio of **2-d_n**:**3-d_n** were observed across experiments (0.70:1 to 0.97:1), mirroring the behaviour of non-deuterated **1**. These variations also influenced the distribution of individual isotopologues and isotopomers within **3-d_n**. For instance, the proportion of *p*-Ph-C-deuterated isotopomers (***XXXD***) differed slightly between batches (19% *vs.* 15% for A and B, respectively), while more pronounced differences were observed for deuteridoborates (***DXXX***; 32.7% *vs.* 52.4%, respectively; *cf.* ^{1}H and ^{11}B NMR spectra of batches A and B shown in Figure S36D,E at page S35 and Figure 8).

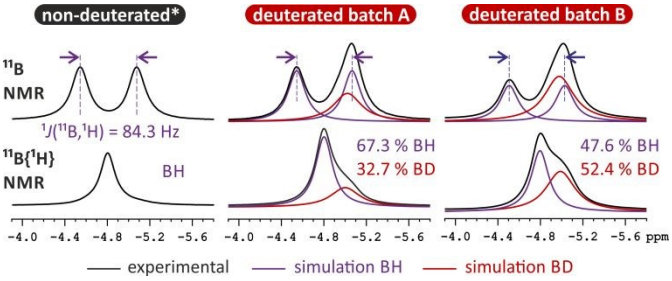

Figure 8: Detailed expansion of the ^{11}B and ^{11}B{^{1}H} NMR spectra (160.48 MHz, THF-d_8, 21 °C) of different batches of the final reaction mixtures (black traces), focused on the signal of borate complex **3-d_n**, showing the distribution of BD (red) and BH (blue) species obtained by signal deconvolution. The proton-coupled ^{11}B spectra were deconvoluted using a doublet splitting of 84.3 Hz. (*) BD is present at natural abundance in this case. Full spectra are provided in the SI.

These discrepancies (in both **2-d_n**:**3-d_n** molar ratio and D-atom enrichment) likely arise from experimental ambiguities associated with the heterogeneous nature of the reaction. Importantly, however, within a given batch, the fraction of *p*-Ph deuterated isotopomers is identical for both **2-d_n** (***_X_D***) and **3-d_n** (***XXXD***) (19 *vs.* 15 % for batches A and B, respectively), indicating the presence of a common intermediate in at least one reaction pathway (*vide infra*).

To enable reliable probabilistic analysis of the reaction mixture — particularly the composition of [**3-d_n**·(18-crown-6)·$(THF)_4$] (n ∈ {0–4}) — all analytical data were therefore obtained from a single batch. As batch B was selected for this purpose, the following discussion of the reaction mechanism is primarily based on these data.

Probabilistic analysis of deuterium distribution in the final products (batch B)

Regarding the consequences of deuteration within the isotopologues of **3-d_n** (n ∈ {0–4}), the weighted average deuterium content in this borate complex was determined to be 2.574 D atoms per molecule for batch B (based on LDI-MS analysis; see Table 1 and SI, Sections 3.3–3.6). This value deviates significantly from the three deuterium atoms expected for the idealised tri-deuterated species **3-d_3** (***DDDH***), assuming a simplified reaction stoichiometry (eq. 1):

2 *eq.* **1-d_2** + 2 *eq.* **K** → **2-*d*** (***_D_H***) + **3-d_3** (***DDDH***) (eq. 1)

based on the assumption of only one and three available deuterium incorporation sites in **2-d_n** and **3-d_n**, respectively. The observed value also differs markedly from the four deuterium atoms corresponding to the tetra-deuterated isotopologue **3-d_4** (***DDDD***).

View Article Online
DOI: 10.1039/D6DT01280A

Table 1: List of isotopologues and corresponding isotopomers, including elemental compositions, experimental and theoretical monoisotopic *m/z* values, and associated mass errors for ions detected in positive- and negative-ion mass spectra of the studied systems. Data are shown for **1** and **1-d_n** (n ∈ {0–2}), and for isolated **3** and **3-d_n** (n ∈ {0–4}) from batch B, obtained as polycrystalline samples of [**3**·(18-crown-6)·$(THF)_4$]) and [**3-d_n**·(18-crown-6)·$(THF)_4$], respectively, using ultrahigh-resolution LDI-MS. Comparison with NMR data is provided for **3** and **3-d_n** (n ∈ {0–4}) analysed directly in the reaction mixture (batch B), which also contains **2** and **2-d_n** (n ∈ {0–2}). Relative abundances of isotopologues in the analysed mixtures were determined from the intensities of the corresponding monoisotopic peaks in the full-scan mass spectra.

[a] Contains deuterium only at natural abundance. [b] Differences between isotopic distributions obtained by LDI-MS and NMR are discussed in the SI. [c] For simplicity, diastereotopic *C3*-methylene H/D atoms in ***XHDX*** and ***XDHX*** for **3-d_n** are not distinguished (i.e. ***XHDX*** ≡ ***XDHX***). (N.A.) not available by the given analytical technique. The most abundant isotopomer for each isotopologue is highlighted in grey.

Compound (isotopologue)		Type of ion	Elemental composition	*m/z* exper.	*m/z* theor.	Mass error [ppm]	Abundance of all isotopo-mers based on LDI-MS / NMR [%]	Isotopomer B	Isotopomer *C3*		Isotopomer *p*-*C*	Isotopomer notation [c]	% of an individual isotopomer based on LDI-MS/MS
1		$[\mathbf{1}+H]^+$	$C_{17}H_{21}NB^+$	250.1766	250.1762	1.6	100 [a]/100 [a]						
Mixture of **1-d_n** (n ∈ {0–2})	**1**	$[\mathbf{1}+H]^+$	$C_{17}H_{21}NB^+$	250.1768	250.1762	2.4	3.7 [b]/ 0.4						
	1-*d*	$[\mathbf{1}\text{-}d+H]^+$	$C_{17}H_{20}DNB^+$	251.1832	251.1824	3.2	6.5 [b]/ 5.9						
	1-d_2	$[\mathbf{1}\text{-}d_2+H]^+$	$C_{17}H_{19}D_2NB^+$	252.1894	252.1887	2.8	89.8 [b]/ 93.7						
3		$[\mathbf{3}-K]^-$	$C_{17}H_{21}NB^-$	250.1777	250.1773	1.6	100 [a]/ 100 [a]						
Mixture of **3-d_n** (n ∈ {0–4}) (batch B)	**3**	$[\mathbf{3}-K]^-$	$C_{17}H_{21}NB^-$	250.1778	250.1773	2.0	0.6 / N.A.	H	H	H	H	***HHHH***	0.6
	3-*d*	$[\mathbf{3}\text{-}d-K]^-$	$C_{17}H_{20}DNB^-$	251.1841	251.1835	2.4	6.9 / N.A.	D	H	H	H	***DHHH***	negligible
								H	D	H	H	***HHDH***	~ 6.9
								H	H	D	H		
								H	H	H	D	***HHHD***	negligible
	3-d_2	$[\mathbf{3}\text{-}d_2-K]^-$	$C_{17}H_{19}D_2NB^-$	252.1903	252.1898	2.0	36.7 / N.A.	H	D	D	H	***HDDH***	~ 33.0
								H	D	H	D	***HHDD***	negligible
								H	H	D	D		
								D	D	H	H	***DHDH***	~ 3.7
								D	H	D	H		
								D	H	H	D	***DHHD***	negligible
	3-d_3	$[\mathbf{3}\text{-}d_3-K]^-$	$C_{17}H_{18}D_3NB^-$	253.1964	253.1961	0.8	46.1 / N.A.	D	D	D	H	***DDDH***	~ 38.9
								D	D	H	D	***DHDD***	negligible
								D	H	D	D		
								H	D	D	D	***HDDD***	~ 7.2
	3-d_4	$[\mathbf{3}\text{-}d_4-K]^-$	$C_{17}H_{17}D_4NB^-$	254.2027	254.2024	1.2	9.7 / ≤ 15.0	D	D	D	D	***DDDD***	9.7
							∑ 100	=					∑ 100

% of ***HXXX*** in batch B based on ^{11}B NMR	47.6	≈	∑ of all ***HXXX*** based on LDI-MS/MS [%]	~ 47.7
% of ***DXXX*** in batch B based on ^{11}B NMR	52.4	≈	∑ of all ***DXXX*** based on LDI-MS/MS [%]	~ 52.3
% of ***XXXD*** in batch B based on ^1H NMR	15.0	≈	∑ of all ***XXXD*** based on LDI-MS/MS [%]	~ 16.9
% of **1** in mixture of **1-d_n** (n ∈ {0–2}) based on ^1H NMR	0.4	≈	∑ of all ***XHHX*** based on LDI-MS/MS [%]	0.6
% of **1-*d*** in mixture of **1-d_n** (n ∈ {0–2}) based on ^1H NMR	5.9	≈	∑ of all ***XHDX*** based on LDI-MS/MS [%]	~ 10.6
% of **1-d_2** in mixture of **1-d_n** (n ∈ {0–2}) based on ^1H NMR	93.7	≈	∑ of all ***XDDX*** based on LDI-MS/MS [%]	~ 88.8

This discrepancy can be rationalised by four closely related factors. First, incomplete *C3*-di-deuteration in the starting material results in an average of only 1.933 D atoms per molecule of **1-d_n** (n ∈ {0–2}), rather than ideal value of 2. Second, partial di-deuteration of the product **2-d_n** (n ∈ {0–2}) leads to the formation of both **2-*d*** (***_D_H***) and **2-d_2** (***_D_D***),

which together account for ~99.6% of all **2-*d*$_n$** isotopologues. The presence of ~15% of **2-*d*$_2$** (**_*D*_*D**) effectively reduces the amount of deuterium available for incorporation into **3-*d*$_n$** by approximately 0.15 D atoms per molecule of **2-*d*$_n$**. Third, the experimentally observed deviation of the molar ratio **2-*d*$_n$**:**3-*d*$_n$** from ideal 1:1 value (0.85:1.00 in batch B; i.e. normalised ratio 0.459:0.541)) further contributes to the imbalance. Assuming that one molecule of **1-*d*$_n$** is required for the formation of each molecule of both **2-*d*$_n$** and **3-*d*$_n$**, the resulting discrepancy between the initial deuterium content and that accounted for in the final products is approximately 0.014 D atoms per molecule of **1-*d*$_n$**. Finally, this small deficit can be attributed to the formation of minor by-products, which remove deuterium from the system, for example as mono-deuterated benzene (C_6H_5D) and other unidentified species formed *via* benzene elimination (see SI for detailed calculations).

Importantly, the slightly higher deuterium content in the starting material compared to that found in the final products **2-*d*$_n$** and **3-*d*$_n$**, indicates that all deuterium atoms present at the "***_X_X***" sites in **2-*d*$_n$** and the "***XXXX***" sites in **3-*d*$_n$** originate exclusively from **1-*d*$_n$**, rather than from the deuterated solvent (THF-d_8). This conclusion is supported by experiments performed in non-deuterated THF (batch C), in which the full set of deuterated isotopomers (***DXXX***, ***XHDX***, ***XDDX***, and ***XXXD***) is still observed (Figure S36F at page S35).

Structural elucidation of dimeric (deuterated) short-lived intermediates α-*d*$_n$, β-*d*$_n$, ω$_1$-*d*$_n$ and ω$_2$-*d*$_n$ (n ∈ {0–4})

In the case of the deuterated system, reduction of **1-*d*$_2$** with potassium generates the radical-anionic species **K$^+$1-*d*$_2$$^{\bullet-}$**, which is expected to undergo dimerization to give the tetra-deuterated dimers **α-*d*$_4$**, **β-*d*$_4$**, **ω$_1$-*d*$_4$** and **ω$_2$-*d*$_4$**. However, as the starting material **1-*d*$_n$** (n ∈ {0–2}) is not fully di-deuterated, the resulting dimers comprise a distribution of isotopologues **α-*d*$_n$**, **β-*d*$_n$**, **ω$_1$-*d*$_n$** and **ω$_2$-*d*$_n$** (n ∈ {0–4}), each associated with a larger set of isotopomers dictated by combinatorial statistics. For clarity, the following discussion focuses on the tetra-deuterated representatives (**α-*d*$_4$**, **β-*d*$_4$**, **ω$_1$-*d*$_4$** and **ω$_2$-*d*$_4$**), which are statistically the most abundant.

Remarkably, deuteration enables experimental structural elucidation of these dimers, as their lifetimes are significantly prolonged compared to their non-deuterated counterparts. While **α**, **β**, **ω$_1$** and **ω$_2$** are detectable by NMR spectroscopy for only ca. 90 minutes at room temperature, the deuterated species **α-*d*$_n$**, **β-*d*$_n$**, **ω$_1$-*d*$_n$** and **ω$_2$-*d*$_n$** remain observable for up to 41 h under identical conditions, with conversion to **2-*d*$_n$** and **3-*d*$_n$** reaching only 84 %. This pronounced lifetime extension upon *C3*-di-deuteration indicates the involvement of a primary kinetic isotope effect (KIE) (*vide infra*). Although quantitative determination of k_H/k_D is precluded by experimental limitations associated with the heterogeneous and tandem nature of the process, the magnitude of the effect (k_H/k_D >>1) clearly supports a primary KIE.

Importantly, *C3*-di-deuteration does not affect the rate of dimerization of **K$^+$1-*d*$_2$$^{\bullet-}$** (i.e., the second stage), which remains extremely fast irrespective of isotopic substitution. The observed apparent KIE therefore pertains exclusively to the subsequent transformation of **α-*d*$_n$**, **β-*d*$_n$**, **ω$_1$-*d*$_n$** and **ω$_2$-*d*$_n$** into the final products **2-*d*$_n$** and **3-*d*$_n$** (the third stage), in which migration of the *C3* methylene H/D atom is both the initiating and rate-determining step (*vide infra*). Notably, the relative molar ratio of the dimers (1:0.98:1.45:1.08 at 21 °C) is identical for both deuterated and non-deuterated systems and remains essentially constant during their conversion to the final products.

The structures of the deuterated intermediates **α-*d*$_4$**, **β-*d*$_4$**, **ω$_1$-*d*$_4$** and **ω$_2$-*d*$_4$** (Scheme 5), which are equally applicable to the non-deuterated analogues and intermediate isotopologues (Scheme 3), were unambiguously established by 2D NMR homo- and heteronuclear NMR correlation experiments and ^{1}H-^{1}H EXSY/NOESY measurements (Figures S36-S49). These dimers arise from Krause–Gomberg-type radical-anion dimerization of **K$^+$1-*d*$_2$$^{\bullet-}$** *via* B(sp^3)-C(sp^3) coupling.

In contrast to the classical Krause dimerization of the achiral $Ph_3B^{\bullet-}$ radical-anion (Scheme 3), which yields essentially a single dimer,[102] the presence of two distinct aromatic coupling sites and the prochiral nature of **K$^+$1$^{\bullet-}$** (and **K$^+$1-*d*$_2$$^{\bullet-}$**) leads to the formation of four structurally distinct dimeric dianions. Each structure contains two distinct boron environments, denoted as a tetrahedral (T_d) and a planar boron unit, their respective coordination geometries (Scheme 5).

The exclusive formation of B(sp^3)-C(sp^3) coupled dimers, involving the pyramidalized boron atom of one monomer and either the *C5* position of the dearomatized *2,1-Bab* ring (**α-*d*$_4$** and **β-*d*$_4$**) or the *para*- position of the dearomatized *B*-phenyl substituent (**ω$_1$-*d*$_4$** and **ω$_2$-*d*$_4$**) of the second monomer of **K$^+$1-*d*$_2$$^{\bullet-}$**, can be rationalised by two factors: minimization of steric repulsion and localization of SOMO alpha-spin density at these sites (Figure 6). Formation of B(sp^3)-B(sp^3) coupled dimers is likely disfavoured by steric congestion arising from the *B*-phenyl-*N*-*tert*-butyl substitution pattern. Similar steric constraints are known to prevent formation of hexaphenylethane in Gomberg-type systems,[103] except in highly specialised or constrained cases.[116-118]

Alternative C–C coupling pathways (e.g., so-called *p,p'*-dimers)[119] are also not observed (see Section 3.1 in SI). While such species have been proposed in related systems,[102] their absence here is likely due to thermodynamic destabilization associated with simultaneous dearomatization of two C_6 rings,[118] in contrast to the observed dimers, which involve only a single dearomatized ring.

View Article Online
DOI: 10.1039/D6DT01280A

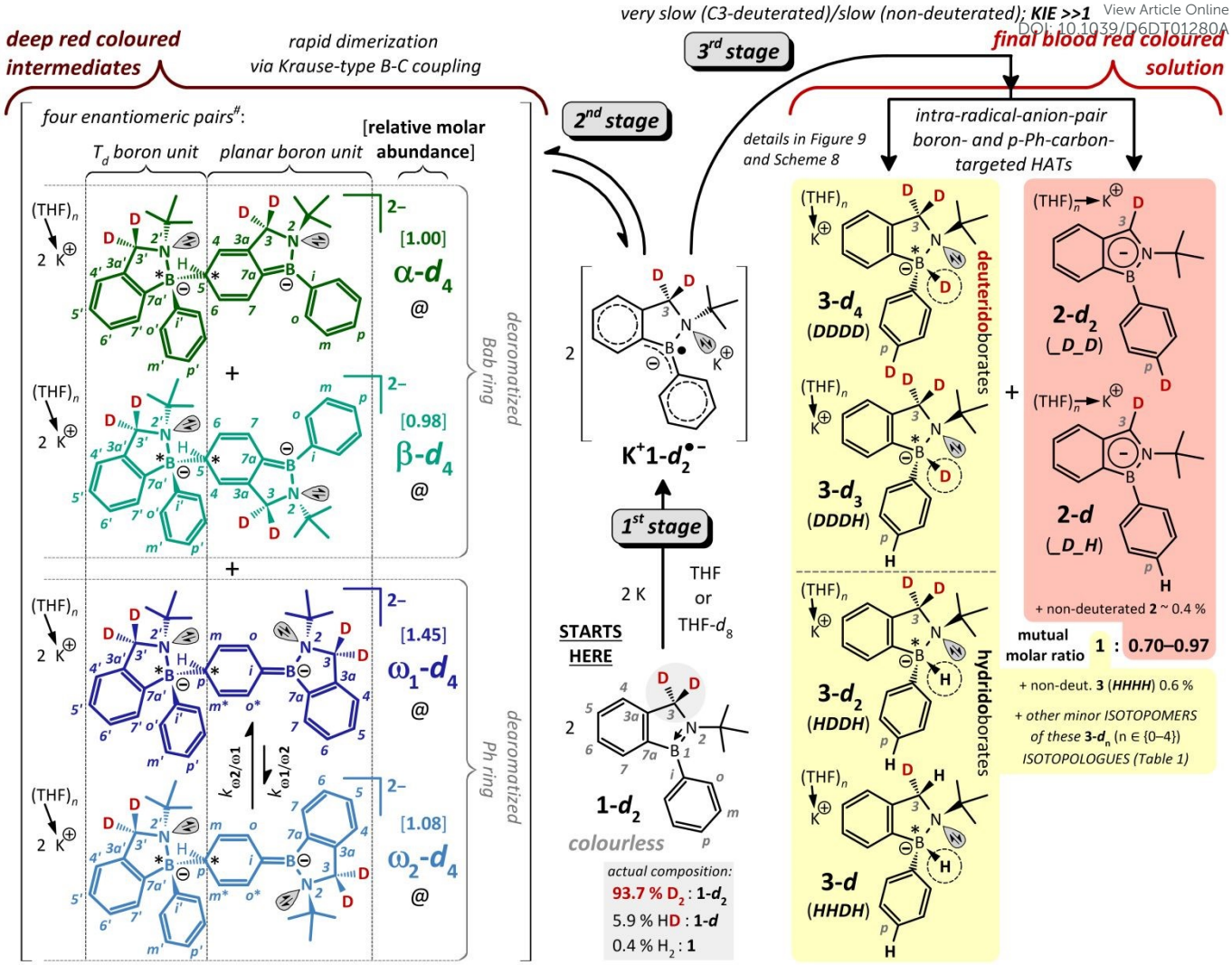

Scheme 5: Overview of the reduction of *C3*-di-deuterated 1*H*-2,1-benzazaborole derivative **1-d_n** (n ∈ {0–2}) by potassium metal in THF/THF-d_8, depicting the proposed structures of the short-lived intermediates **α-d_4**, **β-d_4**, **ω$_1$-d_4** and **ω$_2$-d_4**, and the formation of the final products **2-d_n** (n ∈ {0–2}) and **3-d_n** (n ∈ {0–4}). (#) Each of the intermediates **α-d_4**, **β-d_4**, **ω$_1$-d_4** and **ω$_2$-d_4** is formed as a racemate; thus, a total of eight stereoisomeric intermediates are present. For clarity, only one enantiomer and the most abundant isotopologue (d_4) are shown in each case. (@) Lower isotopologues of each dimer (e.g. **α-d_3**, **α-d_2**, **α-*d*** and **α**) are also formed, reflecting the initial isotopic composition of the monomer **K$^+$1-$d_n$$^{\bullet-}$** (n ∈ {0–2}). Furthermore, multiple isotopomers are expected for each isotopologue based on combinatorial considerations (*cf.* ^{1}H NMR spectra in Figure S36A and C at page S35).

From a thermodynamic perspective, the relative molar ratio of the dimers reflects a balance between the Gibbs free energies of formation (ΔG_r^0) and the activation barriers ($\Delta G^{\ddagger}$) for dimerization of **K$^+$1$^{\bullet-}$**. DFT calculations (M062X/D3/def2-TZVP (PCM, THF)) identified transition states **TS1-α**, **TS1-β**, **TS1-ω$_1$** and **TS1-ω$_2$** (spin multiplicities M = 1; Figure 9), with $\Delta G^{\ddagger}$ in the range 7.29–12.15 kcal mol^{-1}, consistent with kinetically accessible processes at room temperature. However, the experimentally observed ratio (1:0.98:1.45:1.08) does not directly correlate with calculated ΔG_r^0 values [**α** (−16.45) < **β** (−15.34) < **ω$_2$** (−3.44) < **ω$_1$** (−3.41) kcal mol^{-1}], suggesting the involvement of additional dynamic factors.

Indeed, interconversion between dimers—particularly within the **ω$_1$/ω$_2$** pair—is likely operative. The negligible $\Delta\Delta G_r^0$ (0.03 kcal mol^{-1}) and moderate barriers for reverse monomerization ($\Delta G^{\ddagger}$ ≈ 13.6–15.6 kcal mol^{-1}) indicate facile equilibration between **ω$_1$** and **ω$_2$** *via* reversible dissociation and recombination. This behaviour is supported by ^{1}H-^{1}H EXSY/NOESY experiments at 295 K, which reveal exchange between **ω$_2$** and **ω$_1$** [apparent equilibrium constant *K′*(**ω$_2$-d_4**⇌**ω$_1$-d_4**) = 1.34; mixing time 0.9 s; Figures S40 and S41].

The observed relative molar distribution of dimers in NMR spectra therefore most likely reflects a dynamic equilibrium between the radical-anionic precursor **K$^+$1$^{\bullet-}$** and the ensemble of dimeric species (Scheme 6). The absence of an EPR signal for the deep red solution, combined with well-resolved NMR spectra, suggests either an extremely low steady-state concentration of **K$^+$1$^{\bullet-}$** or its association into ion-pair clusters, analogous to behaviour reported for M$^+$Ph$_3$B$^{\bullet-}$ (the Krause's Adduct monomer; M = alkali metal) in ethereal solvents.[8, 120]

$$2\left[\mathbf{K^+1^{\bullet-}}\right] \rightleftharpoons \left[1.00\,\alpha + 0.98\,\beta + 1.45\,\omega_1 + 1.08\,\omega_2\right]$$

$$2\left[\mathbf{K^+1\text{-}}d_2^{\bullet-}\right] \rightleftharpoons \left[1.00\,\alpha\text{-}d_4 + 0.98\,\beta\text{-}d_4 + 1.45\,\omega_1\text{-}d_4 + 1.08\,\omega_2\text{-}d_4\right]$$

Scheme 6: Proposed dynamic equilibrium between (non-)deuterated metastable dimers and the corresponding radical-anionic species **K$^+$1-$d_n$$^{\bullet-}$** (n = 0 or 2) in THF.

View Article Online
DOI: 10.1039/D6DT01280A

From the NMR perspective, the characteristic signals observed in the deep red solution arise from the quinoid structures of the dearomatized benzene rings, namely the *2,1-Bab* moiety in **α** and **β**, and *B*-phenyl rings in **ω₁** and **ω₂**. These structural motifs give rise to two four-membered and two five-membered spin systems, respectively, which are responsible for the distinctive doublet-like signals in the ^{1}H NMR spectra in the range of 3.3–6.3 ppm (Figure 4 and Figure S36A,C at page S35).

As **ω₁** and **ω₂** are structurally related to Krause's Adduct (KA, Scheme 3),[102] the corresponding ^{1}H NMR patterns of their quinoid rings are in good agreement [*cf. p*-H: 3.39 (**ω₁**) and 3.33 (**ω₂**) *vs.* 4.03 ppm for KA; *m*- and *m**-H: 4.96–5.08 ppm (**ω₁** and **ω₂**) *vs.* 5.39 ppm for KA; *o*- and *o**-H: 6.17–6.73 ppm (**ω₁** and **ω₂**) *vs.* 6.58 ppm for KA]. Due to near-complete di-deuteration at the *C3* and *C3'* positions, the eight methylene AX spin system systems (corresponding to these positions in the four dimers), which appear for non-deuterated **α**, **β**, **ω₁** and **ω₂** in the range 3.5–4.6 ppm (*cf.* Figure S36A *vs.* C), are almost entirely suppressed in the ^{1}H NMR spectra of **α-*d*ₙ**, **β-*d*ₙ**, **ω₁-*d*ₙ** and **ω₂-*d*ₙ** (n ∈ {0–4}) (see Section 2.12.3 in SI for full assignment).

Notably, NMR spectroscopy enables a surprisingly detailed structural characterisation of the deuterated dimers in solution. In addition to ^{1}H-^{1}H NOESY experiments (Figures S40 and S41), the high sensitivity of ^{15}N chemical shifts to subtle structural and electronic changes proved particularly informative. Upon B(sp³)-C(sp³) coupling, a boron-carbon double bond is established in the planar boron unit of each dimer, i.e., either *C7a*=B1 (**α-*d*ₙ** and **β-*d*ₙ**) or *i*-C=B (**ω₁-*d*ₙ** and **ω₂-*d*ₙ**). As a consequence, the boron *p*-orbital is no longer fully available for pπ-pπ interaction with nitrogen, leading to partial disruption of the B(sp²)–N(sp²) double-bond character present in the starting material **1-*d*ₙ** [δ(^{15}N) = −238.3 ppm].

This redistribution of bonding results in partial pyramidalization of the nitrogen atom in the planar boron unit. Indeed, the ^{1}H-^{15}N HMBC spectrum (Figure S49) reveals, in addition to signals for the final products **2-*d*ₙ** and **3-*d*ₙ** at δ(^{15}N) = −209.5 and −333.3 ppm, respectively, eight additional signals corresponding to the four dimers. These can be grouped into two distinct sets, both within the typical range for pyramidal amines: δ(^{15}N) = −341.6, −342.0, −342.3, and −341.6 ppm (N' atoms in the T_d boron units) and −294.2, −294.4, −290.3, and −290.6 ppm (N atoms in the planar boron units) for of **α-*d*ₙ**, **β-*d*ₙ**, **ω₁-*d*ₙ** and **ω₂-*d*ₙ**, respectively.

These values indicate full pyramidalization at the nitrogen atoms of the tetrahedral boron units, whereas the nitrogen atoms in the planar boron units remain only partially pyramidalized, consistent with residual pπ-pπ interaction with the adjacent boron centre. This bonding picture is fully supported by DFT-optimised structures. In all four dimers, the N–B bond length within the planar boron unit (1.473, 1.461, 1.479, and 1.472 Å, respectively) is significantly shorter than that in the tetrahedral unit distance (1.560, 1.562, 1.613, and 1.612 Å, respectively; *cf.* Σ_{rcov}(N-B) = 1.56 Å[94]).

DFT calculations further confirm the quinoid, dearomatized nature of the C_6 rings in both the *2,1-Bab* moiety (**α** and **β**) and the *B*-phenyl substituent (**ω₁** and **ω₂**), as evidenced by alternating C–C bond lengths and partial C=B double-bond character. In **ω₁** and **ω₂**, the (*i*-C)=B bond length is 1.501 Å (*cf.* Σ_{rcov}(C-B) = 1.60 Å[94]), while in **α** and **β**, the (*C7a*)=B1 bond is shortened from 1.564 Å in **1** to 1.489 Å (**α**) and 1.494 Å (**β**) (*cf.* Σ_{rcov}(C=B) = 1.45 Å[94]).

Finally, the central B(sp³)-C(sp³) bond, which connects the tetrahedral and planar boron units in all dimers, is only slightly elongated (1.675–1.687 Å) relative to the sum of covalent radii (Σ_{rcov}(C-B) = 1.60 Å[94]), consistent with the observed propensity for reversible monomerization.

Conversion of dimeric intermediates α-*d*ₙ, β-*d*ₙ, ω₁-*d*ₙ and ω₂-*d*ₙ into 2-*d*ₙ and 3-*d*ₙ: third stage of the reaction

Under the assumption that the H/D distribution at the boron atom, the *C3* carbon, and the *p*-Ph carbon in the final products **2-*d*ₙ** (n ∈ {0–2}) and **3-*d*ₙ** (n ∈ {0–4}) remains invariant, it is, in principle, possible to reconstruct the third stage of the tandem mechanism, i.e., the transformation of the dimers into the final products. This reconstruction is based on experimental data obtained for batch B and on the following seven key observations.

First, starting compound **1-*d*ₙ** (n ∈ {0–2}) is no longer present at this stage of the reaction, excluding its direct involvement in reactions with the dimeric intermediates **α-*d*ₙ, β-*d*ₙ, ω₁-*d*ₙ** and **ω₂-*d*ₙ** (n ∈ {0–4}). Second, a primary kinetic effect (KIE) is observed for the conversion of the *C3*- and *C3'*-deuterated dimers into **2-*d*ₙ** and **3-*d*ₙ**, indicating that H/D transfer from the *C3*/*C3'* methylene positions (formally; *vide infra*) is both the initiating and rate-determining step of the third stage, and thus of the overall mechanism. Third, from a stoichiometric perspective, **3-*d*ₙ** contains one H/D atom more than the radical-anionic precursor **K⁺1-*d*ₙ•⁻**, whereas **2-*d*ₙ** contains one fewer, meaning that the two products differ by two H/D atoms.

Fourth, the distribution of deuterium at the *C3* methylene in **3-*d*ₙ**, reflected by the relative abundance of ***XHHX*** (~0.6%), ***XHDX*** (~10.6%), and ***XDDX*** (~88.8%) isotopomers (derived from LDI-MS analysis), closely mirrors that of the starting material **1-*d*ₙ** (0.4% **1**, 5.9% **1-*d***, and 93.7% **1-*d*₂**, based on NMR integration; Table 1), and is thus inherited from the corresponding radical-anionic species **K⁺1-*d*ₙ•⁻**. Fifth, although the formation of multiple isotopomers of **3-*d*ₙ** (n ∈ {0–4}) is expected from the isotopic composition of **1-*d*ₙ** (n ∈ {0–2}), the relatively high proportion of hydridoborates ***HXXX*** (47.7% from LDI-MS) compared to deuteridoborates ***DXXX*** (52.3%) cannot be explained solely on this basis. Instead, it points to the involvement of multiple competing pathways in the third stage. At least one non-trivial pathway must involve additional H/D migration steps leading to *p*-Ph deuterated ***_X_D*** isotopomer of **2-*d*ₙ** and ***XXXD*** isotopomers of **3-*d*ₙ**, where each D incorporation at the *p*-Ph position generates a corresponding H atom, contributing to the observed enrichment of ***HXXX*** species.

Sixth, the observation that, in addition to boron, the *p*-Ph carbon serves as a destination for deuterium in both **2-*d*ₙ** and

View Article Online DOI: 10.1039/D6DT01280A

3-d_n suggests the presence of at least two parallel reaction pathways. Seventh, the identical proportion of *p*-Ph-deuterated ***_X_D*** and ***XXXD*** isotopomers in both products (15 %) strongly indicates a shared intermediate or branching point in the mechanism.

Taken together, these findings support a paramagnetic rather than a diamagnetic reaction pathway for the transformation of dimers into **2-d_n** and **3-d_n**, despite the diamagnetic nature of both intermediates and products. In this scenario, the dimers undergo reversible monomerization to yield pairs of radical-anionic species **K^+1-$d_n^{\bullet-}$**, which, upon suitable mutual orientation, engage in intermolecular H/D transfer. Specifically, an H/D atom from the *C3* methylene group of a donor unit is transferred either to the boron atom B1' of an acceptor unit, leading to the formation of **3-d_n** (more probable pathway), or to the *p'*-Ph carbon, followed by further H/D migrations (less probable pathway; *vide infra*).

Hydrogen atom transfer (HAT) generally involves the concerted transfer of a proton and an electron in a single kinetic step.[121, 122] While examples of HAT between organic substrates and transition metal centres are known,[123, 124] such processes have not previously been reported in connection with Gomberg-type dimers. Moreover, boron-targeted HAT represents a rare class of transformations. This type of process was studied in detail by Roberts et al. in the 1990s in the context of radical scrambling involving neutral amine–boryl radicals generated from amine-boranes.[125-127] Related systems include diradical dianionic boron compounds reported by Wang *et al.*,[17] radical cationic diazadiborinines described by Kinjo,[51] and diborane radical anions investigated by Furukawa, Lin, and Yamashita.[128] In most of these cases, however, the mechanistic details of hydrogen transfer were not the primary focus. More recent studies invoking HAT in boron chemistry typically involve boron as an indirect mediator rather than as the acceptor centre itself,[129-131] or describe H-atom abstraction from B–H bonds in NHC–borane complexes.[132-134]

To evaluate the viability of the proposed mechanism for the third stage, DFT calculations were performed on the non-deuterated system to identify relevant transition states (TS) and intermediates (INT). A low-energy transition state **TS2** (spin multiplicity M = 1, $\Delta G^{\ddagger}$ = 10.90 kcal mol^{-1}) corresponding to boron-targeted HAT was located (Figure 9). This pathway provides a direct route to the formation of **2** and **3**, although alternative pathways are also accessible (*vide infra*). In **TS2**, the H atom is transferred from the *C3* carbon atom to the boron atom *B1'*, which are separated by 3.114 Å. This process is assisted by a potassium cation that bridges the donor unit *via* coordination to the nitrogen lone pair and the *C3* carbon, and the acceptor unit *via* interaction with π-system of the B1'-phenyl group.

The *C3*···H···*B1'* arrangement in **TS2** is nearly linear (162.0°), closely resembling the geometry reported by Roberts et al. for boron-targeted HAT (> *C*···H···*B* = 159.9°).[125] Thus, in **TS2**, the near-linearity of this arrangement appears to be an intrinsic feature of the HAT process, only marginally perturbed by additional interaction between the bridging H atom and the potassium cation. The H atom also interacts with the potassium cation at a distance of 2.628 Å (cf. Σ_{rvdW}(K···H) = 3.85 Å[135]; Σ_{rcov}(K-H) = 2.28 Å[94]). A second potassium cation coordinates to B1' from the opposite side, aligning with the *C3*···H···*B1'* axis (> *C3*···*B1'*···K = 157.7°), thereby further stabilising the transition state. The driving force for this "intra-radical-anion-pair boron-targeted HAT" is likely a synergistic combination of aromatization of the five-membered C_3BN ring in the donor unit (leading to **2**) and the thermodynamic stabilisation of the borate complex **3**, as reflected in the large exergonicity of the process (ΔG_r^0 = −40.84 kcal mol^{-1}).

Importantly, the structure of **TS2** implies that dimers **α**, **β**, **ω_1** and **ω_2** must first undergo reverse monomerization *via* homolytic cleavage of the *C5*–*B1'* (**α** and **β**) or at (*p*-C)–*B1'* bond (**ω_1** and **ω_2**), regenerating two molecules of **K^+1$^{\bullet-}$** through the corresponding **TS1** transition states. These species can subsequently reorient to access **TS2**, enabling the boron-targeted HAT from *C3* to *B1'* (Figure 9). However, because the associated activation barriers are comparable ($\Delta G^{\ddagger}$ = 10.90 kcal mol^{-1} for **TS2** *vs.* 7.29–12.15 kcal mol^{-1} for **TS1**s), the re-formed radical-anion pair can either proceed toward product formation or recombine to regenerate any of the dimers with similar probability (Scheme 7).

This dynamic interplay renders the mechanism inherently non-linear (Figure 9). In this context, the dimers act as a transient "buffer reservoir" for the highly reactive **K^+1$^{\bullet-}$** species, prolonging its effective lifetime through rapid reversible interconversion and thereby extending the overall reaction timescale to hours.

View Article Online
DOI: 10.1039/D6DT01280A

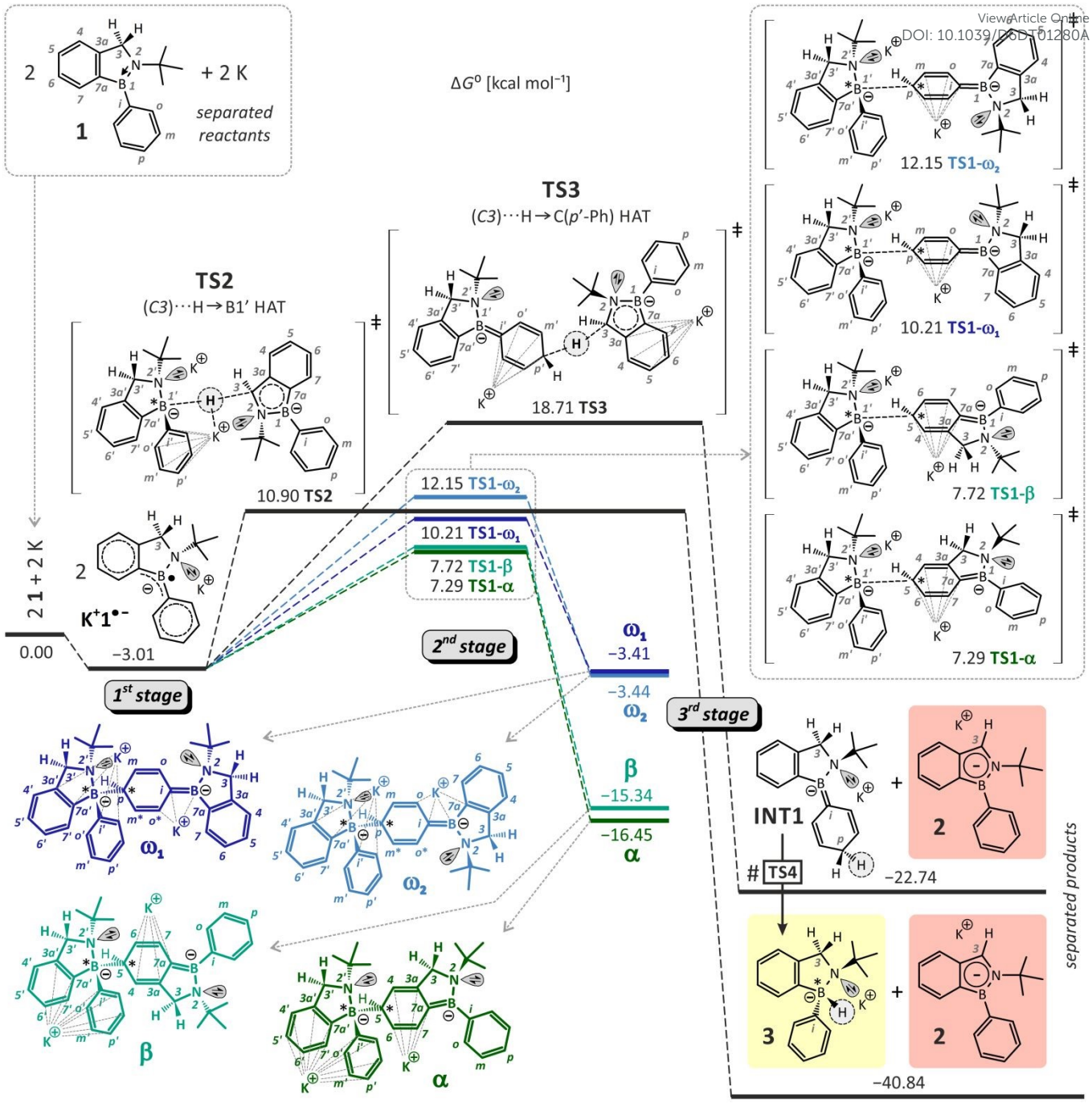

Figure 9: DFT-calculated energy profile (M062X/D3/def2-TZVP (PCM, THF)) for the overall non-linear tandem reaction of **1** upon reduction with potassium metal based on various H-atom transfers (HATs). All transition states (TS), dimeric intermediates, and the final product **3** are formed as pairs of enantiomers; for clarity, only one enantiomer is shown. (#) For the transformation of **INT1** into **3** via **TS4**, see Scheme 8. Cartesian coordinates of all optimised structures are provided in the SI (xyz file).

When the deuterated precursor **1-*d*ₙ** (n ∈ {0–2}) is employed, the pathway *via* **TS2** is directly reflected in the isotopologue distribution of the final products. In the dominant case of **1-*d*₂** (93.7% content by NMR), formation of **K⁺1-*d*₂•⁻** followed by HAT through **TS2** yields ***_D_H*** isotopomer of **2-*d*** together with the ***DDDH*** isotopomer of **3-*d*₃** (Scheme 7B). Consistently, **3-*d*₃** (***DDDH***) is indeed both the most abundant isotopologue and isotopomer observed (Table 1). Its experimentally observed abundance (38.9% by LDI-MS), however, falls well below the idealized limit, which can be attributed not only to incomplete deuteration of the starting material but, more importantly, to the operation of additional competing pathways alongside **TS2** (Scheme 7A**;** *vide infra*).

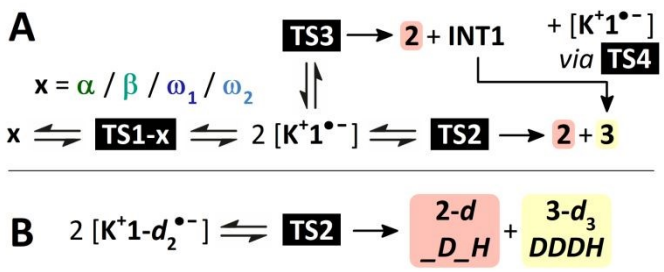

Scheme 7: Diagrams related to Figure 9 illustrating the transformation of **TS1**s states of non-deuterated dimers **α**, **β**, **ω₁** and **ω₂** into **TS2** *via* transient formation of two **K⁺1•⁻** species, leading to the formation of final products **2** and **3**, alongside the **TS3** → **TS4** pathway discussed later in this manuscript (A), and the outcome of the **TS2** pathway for **K⁺1-*d*₂•⁻** (B).

The second proposed HAT pathway, targeting not the boron atom but the carbon atom in the *p'*-Ph position of the H-abstractor monomer **K⁺1•⁻**, was also found to be viable, as indicated by the calculated **TS3** (M = 1, $\Delta G^{\ddagger}$ = 18.71 kcal mol^{-1}; Figure 9). Similarly to **TS2**, the **TS3** becomes accessible after reorientation of two **K⁺1•⁻** units regenerated from any of the **TS1**s pathways. HAT from *C3* methylene group *via* **TS3** leads to formation of the final product **2** along with intermediate **INT1**, with ΔG_r^0 = −22.74 kcal mol^{-1} (Figure 9).

The arrangement of the *C3*···H···(*p'*-Ph-*C*) atoms in **TS3** is even closer to linear than in **TS2** (> *C3*···H···(*p'*-Ph-*C*) = 171.0°), and the boundary atoms-distance is shorter (*C3*···(*p'*-Ph-*C*) = 2.883 Å in **TS3** *vs. C3*···*B1'* = 3.114 Å in **TS2**). Unlike in **TS2**, no potassium cation is bridging H-donor and H-abstractor molecule of the monomer **K⁺1•⁻** in the **TS3**, yet one potassium cation bridges the H-donor and H-abstractor units; however, one potassium cation η⁶-coordinates to the B1'-phenyl ring from the opposite side of the H-atom acceptor, aligned along the axis of the nearly linear *C3*···H···(*p'*-Ph-*C*) arrangement (> *C3*···(*p'*-Ph-*C*)···K = 168.0°).

View Article Online
DOI: 10.1039/D6DT01280A

Upon HAT to the (*p'*-Ph)CH fragment, the phenyl ring in the **INT1** acquires a cross-conjugated diene character as a (*p*-Ph)CH_2 methylene bridge is formed, while the boron atom becomes negatively charged due to π-interaction with the *ipso*-phenyl carbon, giving a trigonal planar borate species. As **INT1** is thermodynamically less stable than the final tetrahedral borate complex **3** by 18.10 kcal mol^{-1}, yet represents its positional isomer, it is subsequently converted into **3** *via* intermolecular, self-propagating cycle involving **TS4** (Scheme 8A).

This step corresponds to a boron-targeted HAT from the (*p*-Ph)CH_2 methylene group of **INT1** to the boron atom of another **K⁺1•⁻** unit ($\Delta G^{\ddagger}$ = 19.44 kcal mol^{-1}). In this process, **INT1** reacts with **K⁺1•⁻** to regenerate a new **K⁺1•⁻** species, effectively propagating the reactive intermediate pool and further contributing to the non-linear character of the overall mechanism. In **TS4**, the key geometric parameters closely resemble those in **TS2**; however, in this case both potassium cations are positioned along the extension of the (*p*-Ph-*C*)···H···*B1'* axis.

The isomerization of **INT1** *via* **TS4** is crucial for rationalizing the formation of *p*-Ph-deuterated isotopomer, namely ***_D_D*** in **2-*d*₂** and ***XXXD*** in **3-*d*ₙ**, when deuterated starting compound material **1-*d*ₙ** is employed (Table 1). In the simplified case of **1-*d*₂** leading to **K⁺1-*d*₂•⁻**, the **TS3** pathway generates a (*p*-Ph)CH,D methylene unit in tri-deuterated **INT1-*d*₃** (Scheme 8B). During subsequent conversion *via* **TS4** in the presence of **K⁺1-*d*₂•⁻**, primary KIE governs the intermolecular competition, favouring transfer of the weaker C–H bond over C–D. This results in formation of the key *p*-Ph-deuterated radical-anion **K⁺1-*d*₃•⁻** along with the ***HDDH*** isotopomer of **3-*d*₂**.

View Article Online
DOI: 10.1039/D6DT01280A

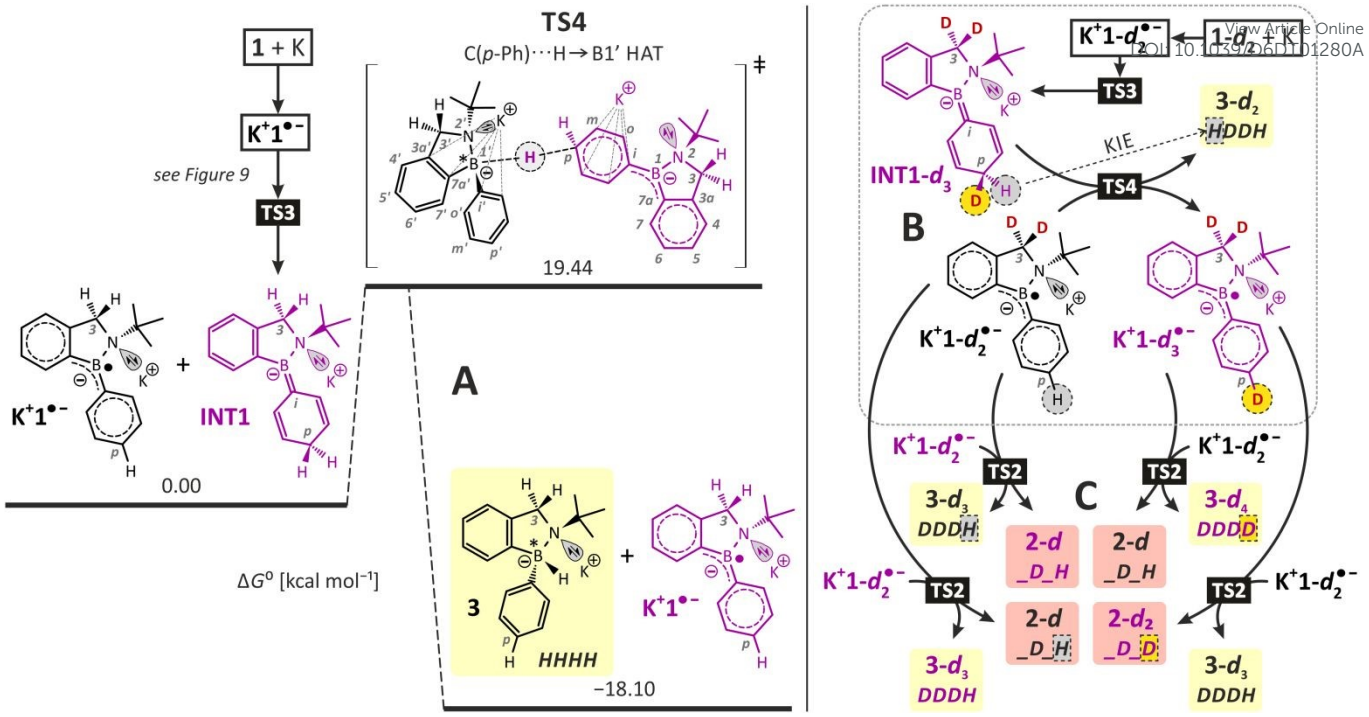

Scheme 8: DFT-calculated energy profile (M062X/D3/def2-TZVP (PCM, THF)) for the isomerization of **INT1** to **3** *via* an intermolecular self-propagating, boron-targeted HAT cycle, leading to propagation of **K⁺1•⁻** (colour change from black to magenta) (A). Corresponding scheme for **INT1-*d*₃**, yielding hydridoborate **3-*d*₂** (***HDDH***) and propagating tri-deuterated **K⁺1-*d*₃•⁻**, assuming **1-*d*₂** as the starting compound (B). Plausible pathways rationalising formation of **3-*d*₄** (***DDDD***) and **2-*d*₂** (***_D_D***) *via* reversal of the boron-targeted D-atom transfer (DAT) through **TS2** (C, right).

The formation of **K⁺1-*d*₃•⁻** in turn explains the origin of the ***_D_D*** isotopomer of **2-*d*₂**, as this species can react with **K⁺1-*d*₂•⁻** *via* the energetically preferred **TS2** pathway, yielding **2-*d*₂** (***_D_D***) together with **3-*d*₃** (***DDDH***) (Scheme 8C). Conversely, reversing the direction of deuterium transfer through **TS2** also accounts for the formation of the tetra-deuterated isotopologue **3-*d*₄** (***DDDD***), with **2-*d*** (***_D_H***) as the corresponding co-product.

Because the *p*-Ph-deuterated isotopomers of both products (i.e., ***_X_D*** in **2-*d*ₙ** and ***XXXD*** in **3-*d*ₙ**) are formed in identical proportions (15% in batch B), the directionality of deuterium transfer between tri-deuterated **K⁺1-*d*₃•⁻** and di-deuterated **K⁺1-*d*₂•⁻** must be statistically equivalent. The validity of the **TS3** → **TS4** → **TS2** sequence is further supported by the experimental observation that these *p*-Ph-deuterated species indeed constitute a minor fraction (~15%) of the product distribution.

Consistently, **3-*d*₂** is the second most abundant isotopologue (36.7% by LDI-MS), and its ***HDDH*** isotopomer is likewise the second most abundant individual isotopomer (33.0%) within the entire **3-*d*ₙ** (n ∈ {0–4}) distribution (Table 1). This agrees with the dominance of the **TS2** pathway ($\Delta G^{\ddagger}$ = 10.90 kcal mol^{-1}), which directly yields **3-*d*₃** (***DDDH***) without requiring additional steps, whereas formation *via* **TS3** necessitates subsequent transformation through higher-energy pathways.

A more detailed discussion of minor isotopomers, as well as deviations in hydridoborate/deuteridoborate ratios, non-ideal **2-*d*ₙ**:**3-*d*ₙ** stoichiometry, and formation of benzene/mono-deuterated benzene as a negligible side product, is provided in the SI (Sections 3.6–3.10).

Although the preceding discussion emphasized the role of dimeric intermediates **α**, **β**, **ω₁** and **ω₂**, the DFT energy profile (Figure 9) indicates that their involvement is not essential. Two molecules of **K⁺1•⁻** formed after the first stage can undergo HAT *via* **TS2** or **TS3** directly, without prior dimerization (**TS1**s) and subsequent monomerization. This is enabled by a shared region on the potential energy surface, where **TS1**s, **TS2** and **TS3** originate from the same pair of **K⁺1•⁻** pair and exhibit comparable activation barriers.

Experimental observations support this scenario. A relatively high degree of conversion to **2** and **3** is observed immediately after complete consumption of potassium, even at low temperature, when the concentration of dimers is maximal. This behaviour is inconsistent with the relatively slow rate of dimer transformation (third stage), particularly evident in deuterated systems (Figure S36C and Section 3.2 in the SI).

Moreover, the relative ratio of **α**, **β**, **ω₁** and **ω₂** (1.00:0.98:1.45:1.08) remains essentially constant during the reaction as it only changes to 1.00:0.93:1.57:1.01 after 41 h (for batch A), indicating similar apparent rate constants and comparable access of all dimers to **TS2** and **TS3** (followed by **TS4**).

Finally, the key factor governing all three HAT processes (**TS2**–**TS4**) is the distribution of SOMO alpha-spin density in **K⁺1•⁻** (Figure 6). The highest contribution is located at the boron atom (relevant for **TS2** and **TS4**), while the second highest resides at the *p*-Ph carbon (relevant for **TS3**). Notably,

the absence of significant spin density at the *C3* methylene position (the H-donor) of $K^+1^{\bullet-}$, or at the (*p*-Ph)CH_2 unit of diamagnetic **INT1**, does not preclude HAT, as such localisation is not a general requirement for this mechanism.[121]

Conclusions

We have carried out a comprehensive mechanistic investigation of the anomalous reduction of 1-Ph-2-*tert*-butyl-1*H*-1,2-benzazaborole (**1**) with potassium in THF. Although **1** is formally isoelectronic with 1*H*-indene derivatives and furnishes isoelectronic products upon reduction, we demonstrate that the underlying reaction pathways are fundamentally different. Whereas substituted 1*H*-indenes follow a self-protonation pathway, compound **1** undergoes a radical disproportionation process mediated mostly by a rare, boron-targeted hydrogen atom transfer (HAT), a rarely documented elementary step and one that is previously unrecognized in such systems. This process yields the known aromatic 2,1-*Bab*$^-$ salt[90, 91] alongside a previously unknown hydridoborate complex **3**.

Mechanistically, the reaction proceeds through an unusual non-linear tandem network. Initial single-electron transfer generates the elusive radical anion $K^+1^{\bullet-}$, which rapidly dimerizes into four Gomberg-type (or Krause-Adduct-type) intermediates **α**, **β**, ω_1 and ω_2. These dimers are not productive endpoints but metastable reservoirs of $K^+1^{\bullet-}$. Their reversible monomerization regenerates radical-anion pairs that undergo selective HAT from the *C3* methylene position to either boron (dominant pathway) or the *para*-phenyl carbon (minor pathway). The latter proceeds *via* intermediate **INT1** and a subsequent intermolecular HAT isomerization cycle. The overall transformation is strongly exergonic, driven by aromatization of the C_3BN ring and formation of a thermodynamically stable borate complex. Reversibility, rapid reorientation, and partial propagation of $K^+1^{\bullet-}$ collectively render the mechanism intrinsically non-linear.

Deuterium-labelling experiments were decisive, enabling the experimental elucidation of the structures of the dimeric intermediates **α**, **β**, ω_1 and ω_2 and confirming the *C3* methylene group as the main source of the hydrogen atom delivered to boron *via* HAT in the formation of **3**. Critically, they also uncovered a second, otherwise hidden HAT pathway targeting the *para*-phenyl position, which would remain obscured in the absence of isotopic labelling due to hydrogen scrambling. The observed selectivity is consistent with the computed spin-density distribution in $K^+1^{\bullet-}$, with HAT occurring preferentially at sites of highest spin density.

Finally, this work establishes that HAT processes can operate within Gomberg-type dimers and Krause-like adducts, a reactivity mode not previously recognized. These findings redefine the mechanistic landscape of such systems and open new perspectives for the rational design of unconventional boron hydrides and related radical processes.

Author contributions

M. H. conceived and supervised the project, designed and performed the synthetic experiments, characterised the compounds, performed the probabilistic calculations, proposed the mechanism, and wrote the manuscript. L. D. acquired funding, contributed to project supervision, and revised the manuscript. O. M. performed the initial mechanistic DFT and TD-DFT calculations. A. R. acquired funding and collected and solved the *sc*-XRD data. A. L. measured and analysed the ^{2}H NMR data. T. M. performed and analysed the electrochemical measurements. R. J. performed and analysed the LDI-MS measurements. M. A. S. designed and carried out the computational studies, contributed key mechanistic insight, and revised the manuscript. All authors have approved the final version of the manuscript.

Conflicts of interest

There are no conflicts to declare.

Acknowledgements

The Grant Agency of the Czech Republic (project No. GA21-02964S) is acknowledged for the financial support.

Notes and references

1. A. Fukazawa, J. L. Dutton, C. Fan, L. G. Mercier, A. Y. Houghton, Q. Wu, W. E. Piers and M. Parvez, *Chem. Sci.*, 2012, **3**, 1814-1818.
2. J. He, F. Rauch, M. Finze and T. B. Marder, *Chem. Sci.*, 2021, **12**, 128-147.
3. C. Präsang, M. Hofmann, G. Geiseler, W. Massa and A. Berndt, *Angew. Chem. Int. Ed.*, 2002, **41**, 1526-1529.
4. T. Kupfer, H. Braunschweig and K. Radacki, *Angew. Chem. Int. Ed.*, 2015, **54**, 15084-15088.
5. H. Braunschweig, V. Dyakonov, J. O. C. Jimenez-Halla, K. Kraft, I. Krummenacher, K. Radacki, A. Sperlich and J. Wahler, *Angew. Chem. Int. Ed.*, 2012, **51**, 2977-2980.
6. W. E. Piers, S. C. Bourke and K. D. Conroy, *Angew. Chem. Int. Ed.*, 2005, **44**, 5016-5036.
7. W. Kaim, N. S. Hosmane, S. Záliš, J. A. Maguire and W. N. Lipscomb, *Angew. Chem. Int. Ed.*, 2009, **48**, 5082-5091.
8. Y. Su and R. Kinjo, *Coord. Chem. Rev.*, 2017, **352**, 346-378.
9. H. Budy, J. Gilmer, T. Trageser and M. Wagner, *Eur. J. Inorg. Chem.*, 2020, **2020**, 4148-4162.
10. R. Bertermann, H. Braunschweig, R. D. Dewhurst, C. Hörl, T. Kramer and I. Krummenacher, *Angew. Chem. Int. Ed.*, 2014, **53**, 5453-5457.
11. H. Braunschweig, I. Krummenacher, L. Mailänder, L. Pentecost and A. Vargas, *Chem. Commun.*, 2016, **52**, 7005-7008.
12. W. Yang, K. E. Krantz, L. A. Freeman, D. A. Dickie, A. Molino, G. Frenking, S. Pan, D. J. D. Wilson and R. J. Gilliard Jr., *Angew. Chem. Int. Ed.*, 2020, **59**, 3850-3854.
13. R. Feng, W. Yang, W. Wang, Y. Zhao, G. Tan, L. Zhang and X. Wang, *Chem. Commun.*, 2019, **55**, 12908-12911.

14. X. Jia, J. Nitsch, Z. Wu, A. Friedrich, J. Krebs, I. Krummenacher, F. Fantuzzi, H. Braunschweig, M. Moos, C. Lambert, B. Engels and T. B. Marder, *Chem. Sci.*, 2021, **12**, 11864-11872.
15. R. Kinjo, B. Donnadieu, M. A. Celik, G. Frenking and G. Bertrand, *Science*, 2011, **333**, 610-613.
16. P. Bissinger, H. Braunschweig, A. Damme, C. Hörl, I. Krummenacher and T. Kupfer, *Angew. Chem. Int. Ed.*, 2015, **54**, 359-362.
17. L. Wang, Y. Fang, H. Mao, Y. Qu, J. Zuo, Z. Zhang, G. Tan and X. Wang, *Chem. Eur. J.*, 2017, **23**, 6930-6936.
18. A. Maiti, F. Zhang, I. Krummenacher, M. Bhattacharyya, S. Mehta, M. Moos, C. Lambert, B. Engels, A. Mondal, H. Braunschweig, P. Ravat and A. Jana, *J. Am. Chem. Soc.*, 2021, **143**, 3687-3692.
19. K. K. Hollister, W. Yang, R. Mondol, K. E. Wentz, A. Molino, A. Kaur, D. A. Dickie, G. Frenking, S. Pan, D. J. D. Wilson and R. J. Gilliard Jr., *Angew. Chem. Int. Ed.*, 2022, **61**, e202202516.
20. Y.-J. Lin, W.-C. Liu, Y.-H. Liu, G.-H. Lee, S.-Y. Chien and C.-W. Chiu, *Nat. Commun.*, 2022, **13**, 7051.
21. B. Y. E. Tra, Y. Zhao, A. Molino, Y. Ouyang, C.-L. Deng, C. McAloon, N. D. McMillion, H. Kim, C. Zhang, P. Müller, R. G. Griffin and R. J. Gilliard, Jr., *J. Am. Chem. Soc.*, 2025, **147**, 18431-18437.
22. S. Li, F. Shiri, G. Xu, S.-M. Yiu, H. K. Lee, T. H. Ng, Z. Lin and Z. Lu, *J. Am. Chem. Soc.*, 2024, **146**, 17348-17354.
23. J. Gilmer, H. Budy, T. Kaese, M. Bolte, H.-W. Lerner and M. Wagner, *Angew. Chem. Int. Ed.*, 2020, **59**, 5621-5625.
24. J. Monot, A. Solovyev, H. Bonin-Dubarle, É. Derat, D. P. Curran, M. Robert, L. Fensterbank, M. Malacria and E. Lacôte, *Angew. Chem. Int. Ed.*, 2010, **49**, 9166-9169.
25. Y. Segawa, M. Yamashita and K. Nozaki, *Science*, 2006, **314**, 113-115.
26. Y. Segawa, Y. Suzuki, M. Yamashita and K. Nozaki, *J. Am. Chem. Soc.*, 2008, **130**, 16069-16079.
27. E. Bernhardt, V. Bernhardt-Pitchougina, H. Willner and N. Ignatiev, *Angew. Chem. Int. Ed.*, 2011, **50**, 12085-12088.
28. J. Landmann, J. A. P. Sprenger, R. Bertermann, N. Ignat'ev, V. Bernhardt-Pitchougina, E. Bernhardt, H. Willner and M. Finze, *Chem. Commun.*, 2015, **51**, 4989-4992.
29. J. Landmann, F. Keppner, D. B. Hofmann, J. A. P. Sprenger, M. Häring, S. H. Zottnick, K. Müller-Buschbaum, N. V. Ignat'ev and M. Finze, *Angew. Chem. Int. Ed.*, 2017, **56**, 2795-2799.
30. M. J. S. Dewar, V. P. Kubba and R. Pettit, *J. Chem. Soc. (Resumed)*, 1958, DOI: 10.1039/JR9580003073, 3073-3076.
31. M. J. D. Bosdet and W. E. Piers, *Can. J. Chem.*, 2009, **87**, 8-29.
32. P. G. Campbell, A. J. V. Marwitz and S.-Y. Liu, *Angew. Chem. Int. Ed.*, 2012, **51**, 6074-6092.
33. G. Bélanger-Chabot, H. Braunschweig and D. K. Roy, *Eur. J. Inorg. Chem.*, 2017, **2017**, 4353-4368.
34. A. J. V. Marwitz, M. H. Matus, L. N. Zakharov, D. A. Dixon and S.-Y. Liu, *Angew. Chem. Int. Ed.*, 2009, **48**, 973-977.
35. M. M. Morgan, E. A. Patrick, J. M. Rautiainen, H. M. Tuononen, W. E. Piers and D. M. Spasyuk, *Organometallics*, 2017, **36**, 2541-2551.
36. Y. Zhang, W. Li, R. Jiang, L. Zhang, Y. Li, X. Xu and X. Liu, *J. Org. Chem.*, 2022, **87**, 12986-12996.
37. M. J. D. Bosdet, W. E. Piers, T. S. Sorensen and M. Parvez, *Angew. Chem. Int. Ed.*, 2007, **46**, 4940-4943.
38. J. Li, C. G. Daniliuc, G. Kehr and G. Erker, *Angew. Chem. Int. Ed.*, 2021, **60**, 27053-27061.
39. M. Hejda, A. Lyčka, R. Jambor, A. Růžička and L. Dostál, *Dalton Trans.*, 2014, **43**, 12678-12688.
40. H. V. Ly, T. D. Forster, A. M. Corrente, D. J. Eisler, J. Konu, M. Parvez and R. Roesler, *Organometallics*, 2007, **26**, 1750-1756.
41. H. V. Ly, T. D. Forster, D. Maley, M. Parvez and R. Roesler, *Chem. Commun.*, 2005, DOI: 10.1039/B508152A, 4468-4470.
42. K. E. Krahulic, G. D. Enright, M. Parvez and R. Roesler, *J. Am. Chem. Soc.*, 2005, **127**, 4142-4143.
43. H. V. Ly, H. M. Tuononen, M. Parvez and R. Roesler, *Angew. Chem. Int. Ed.*, 2008, **47**, 361-364.
44. H. V. Ly, J. Moilanen, H. M. Tuononen, M. Parvez and R. Roesler, *Chem. Commun.*, 2011, **47**, 8391-8393.
45. D. Wu, L. Kong, Y. Li, R. Ganguly and R. Kinjo, *Nat. Commun.*, 2015, **6**, 7340.
46. Y. Su, Y. Li, R. Ganguly and R. Kinjo, *Angew. Chem. Int. Ed.*, 2018, **57**, 7846-7849.
47. Y. Su, D. C. Huan Do, Y. Li and R. Kinjo, *J. Am. Chem. Soc.*, 2019, **141**, 13729-13733.
48. H. V. Ly, J. Konu, M. Parvez and R. Roesler, *Dalton Trans.*, 2008, DOI: 10.1039/B802930J, 3454-3460.
49. Y. Mu, Y. Dai, D. A. Ruiz, L. L. Liu, L.-P. Xu, C.-H. Tung and L. Kong, *Angew. Chem. Int. Ed.*, 2024, **63**, e202405905.
50. Y. Su, Y. Li, R. Ganguly and R. Kinjo, *Chem. Sci.*, 2017, **8**, 7419-7423.
51. B. Wang, Y. Li, R. Ganguly, R. D. Webster and R. Kinjo, *Angew. Chem. Int. Ed.*, 2018, **57**, 7826-7829.
52. H. Wang, J. Zhang, Z. Lin and Z. Xie, *Organometallics*, 2016, **35**, 2579-2582.
53. Y. Aramaki, H. Omiya, M. Yamashita, K. Nakabayashi, S.-i. Ohkoshi and K. Nozaki, *J. Am. Chem. Soc.*, 2012, **134**, 19989-19992.
54. J. Seufert, E. Welz, I. Krummenacher, V. Paprocki, J. Böhnke, S. Hagspiel, R. D. Dewhurst, R. Tacke, B. Engels and H. Braunschweig, *Angew. Chem. Int. Ed.*, 2018, **57**, 10752-10755.
55. N. Yuan, T. Zhu, J. Ma, Y. Xue and Y. Liu, *Dalton Trans.*, 2025, **54**, 2257-2260.
56. L. Zhu, Z. Feng and R. Kinjo, *J. Am. Chem. Soc.*, 2024, **146**, 20945-20950.
57. G. Farnia, G. Sandoná, F. Marcuzzi and G. Melloni, *J. Electroanal. Chem. Interfacial Electrochem.*, 1989, **264**, 297-300.
58. G. Capobianco, G. Farnia, G. Sandona, F. Marcum and G. Melloni, *J. Electroanal. Chem. Interfacial Electrochem.*, 1982, **134**, 363-367.
59. G. Farnia, F. Marcuzzi, G. Melloni and G. Sandona, *J. Am. Chem. Soc.*, 1984, **106**, 6503-6512.
60. G. Farnia, G. Sandonà, F. Marcuzzi and G. Melloni, *J. Chem. Soc., Perkin Trans. 2*, 1988, DOI: 10.1039/P29880000247, 247-254.
61. S. Gotta, M. Marchetti, M. Branca and G. Melloni, *J. Chem. Soc., Perkin Trans. 2*, 1994, DOI: 10.1039/P29940000151, 151-155.
62. G. Farnia, F. Marcuzzi, G. Melloni, G. Sandona and M. V. Zucca, *J. Am. Chem. Soc.*, 1989, **111**, 918-923.
63. A. Bosch and R. K. Brown, *Can. J. Chem.*, 1964, **42**, 1718-1735.
64. G. Farnia, J. Ludvík, G. Sandonà and M. G. Severin, *J. Chem. Soc., Perkin Trans. 2*, 1991, DOI: 10.1039/P29910001249, 1249-1254.
65. A. J. Ashe, in *Comprehensive Heterocyclic Chemistry III*, ed. C. A. R. A. R. Katritzky, E. F. V. Scriven, R. J. K. Taylor, Elsevier, 2008, DOI: https://doi.org/10.1016/B978-008044992-0.00417-X, pp. 1189-1224.
66. G. Schmid, in *Comprehensive Heterocyclic Chemistry II*, eds. A. R. Katritzky, C. W. Rees and E. F. V. Scriven, Pergamon, Oxford, 1996, DOI: https://doi.org/10.1016/B978-008096518-5.00075-7, pp. 739-766.
67. G. Schmid, D. Zaika, J. Lehr, N. Augart and R. Boese, *Chem. Ber.*, 1988, **121**, 1873-1880.

68. G. Schmid, W. Meyer-Zaika, R. Boese and N. Augart, *Angew. Chem. Int. Ed.*, 1988, **27**, 952-953.
69. A. J. Ashe and Fang, *Organic Letters*, 2000, **2**, 2089-2091.
70. S.-Y. Liu, I. D. Hills and G. C. Fu, *J. Am. Chem. Soc.*, 2005, **127**, 15352-15353.
71. Z. Liu, J. Xu, W. Ruan, C. Fu, H.-J. Zhang and T.-B. Wen, *Dalton Trans.*, 2013, **42**, 11976-11980.
72. X. Fang and J. Assoud, *Organometallics*, 2008, **27**, 2408-2410.
73. Y. Chen, X. Fang and W. Dan, *Organometallics*, 2016, **35**, 15-19.
74. X. Fang, Y. Deng, Q. Xie and F. Moingeon, *Organometallics*, 2008, **27**, 2892-2895.
75. X. Fang, X. Li, Z. Hou, J. Assoud and R. Zhao, *Organometallics*, 2009, **28**, 517-522.
76. L. Xie, J. Zhang and C. Cui, *Chem. Eur. J.*, 2014, **20**, 9500-9503.
77. S.-Y. Liu, M. M. C. Lo and G. C. Fu, *Tetrahedron*, 2006, **62**, 11343-11349.
78. A. J. Ashe, H. Yang, X. Fang and J. W. Kampf, *Organometallics*, 2002, **21**, 4578-4580.
79. M. M. Morgan, J. M. Rautiainen, W. E. Piers, H. M. Tuononen and C. Gendy, *Dalton Trans.*, 2018, **47**, 734-741.
80. M. Yamashita, Y. Aramaki and K. Nozaki, *New J. Chem.*, 2010, **34**, 1774-1782.
81. C. P. Manankandayalage, D. K. Unruh and C. Krempner, *Chem. Commun.*, 2021, **57**, 12528-12531.
82. M. Beguerie, C. Faradji, L. Vendier, S. Sabo-Etienne and G. Alcaraz, *ChemCatChem*, 2017, **9**, 3303-3306.
83. M. Beguerie, C. Dinoi, I. del Rosal, C. Faradji, G. Alcaraz, L. Vendier and S. Sabo-Etienne, *ACS Catal.*, 2018, **8**, 939-948.
84. H. E. Dunn, J. C. Catlin and H. R. Snyder, *J. Org. Chem.*, 1968, **33**, 4483-4486.
85. M. Lauer and G. Wulff, *J. Organomet. Chem.*, 1983, **256**, 1-9.
86. A. M. Genaev, S. M. Nagy, G. E. Salnikov and V. G. Shubin, *Chem. Commun.*, 2000, DOI: 10.1039/B003999N, 1587-1588.
87. A. Rydzewska, K. Ślepokura, T. Lis, P. Kafarski and P. Młynarz, *Tetrahedron Lett.*, 2009, **50**, 132-134.
88. R. Zhang, Y. D. Zhang, L. X. Wang, C. H. Ge, Z. Y. Ma, J. P. Miao and X. D. Zhang, *Inorg. Chem. Commun.*, 2016, **74**, 52-57.
89. M. Hejda, A. Lyčka, R. Jambor, A. Růžička and L. Dostál, *Dalton Trans.*, 2013, **42**, 6417-6428.
90. M. Hejda, R. Jambor, A. Růžička, A. Lyčka and L. Dostál, *Dalton Trans.*, 2014, **43**, 9012-9015.
91. M. Hejda, A. Lyčka, T. Mikysek, R. Jambor, A. Růžička, J. Vinklárek, C. Wilfer, A. Hoffmann, S. Herres-Pawlis and L. Dostál, *Chem. Eur. J.*, 2016, **22**, 15340-15349.
92. G. Farnia, F. Marcuzzi and G. Sandonà, *J. Electroanal. Chem.*, 1999, **460**, 160-175.
93. C. Amatore, G. Capobianco, G. Farnia, G. Sandona, J. M. Saveant, M. G. Severin and E. Vianello, *J. Am. Chem. Soc.*, 1985, **107**, 1815-1824.
94. P. Pyykkö and M. Atsumi, *Chem. Eur. J.*, 2009, **15**, 186-197.
95. R. L. Luck and E. J. Schelter, *Acta Crystallogr. C*, 1999, **55**.
96. V. D'Anna, L. M. Lawson Daku and H. Hagemann, *J. Alloys Compd.*, 2013, **580**, S122-S124.
97. At −80 °C, the deep red reaction mixture remains stable for at least 24 h, whereas at 50 °C no intermediate colour changes are observed and only the final mixture of **2** and **3** is formed. The reaction also proceeds solvent-free upon melting neat **1** with potassium (see the SI).
98. The reaction is severely disrupted when a PTFE-coated stirring bar is used, leading to formation of a black insoluble residue (likely from PTFE reduction) and a complex mixture of decomposition products. A glass-coated stirring bar or ultrasonic agitation is therefore required. As 2,1-*Bab*$^-$ reacts only slowly with PTFE and [**3**·(18-crown-6)(THF)$_2$] is unreactive, these observations point to the involvement of highly reactive, short-lived intermediates.
99. The reported relative abundances were obtained by averaging multiple integrals for each species.
100. E. Krause, *Ber. Dtsch. Chem. Ges.*, 1924, **57**, 216-217.
101. E. Krause and H. Polack, *Ber. Dtsch. Chem. Ges.*, 1926, **59**, 777-785.
102. J. J. Eisch, T. Dluzniewski and M. Behrooz, *Heteroat. Chem.*, 1993, **4**, 235-241.
103. H. Lankamp, W. T. Nauta and C. MacLean, *Tetrahedron Lett.*, 1968, **9**, 249-254.
104. M. Gomberg, *J. Am. Chem. Soc.*, 1900, **22**, 757-771.
105. M. Gomberg, *J. Am. Chem. Soc.*, 1901, **23**, 496-502.
106. M. Gomberg, *J. Am. Chem. Soc.*, 1914, **36**, 1144-1170.
107. M. Gomberg, *J. Am. Chem. Soc.*, 1902, **24**, 597-628.
108. A. J. Rosenthal, M. Devillard, K. Miqueu, G. Bouhadir and D. Bourissou, *Angew. Chem. Int. Ed.*, 2015, **54**, 9198-9202.
109. A. J. Rosenthal, S. Mallet-Ladeira, G. Bouhadir, E.-D. Sosa-Carrizo, K. Miqueu and D. Bourissou, *Organometallics*, 2018, **37**, 755-760.
110. Our experimental setup did not allow direct generation of the radical anion within the EPR spectrometer. Attempts to generate **1**$^{\bullet-}$ *in situ* and rely on its diffusion into the resonator cavity were unsuccessful, most likely due to its extremely rapid dimerization.
111. The redox potentials of alkali metal amalgams are approximately 1 V less negative than those of the corresponding pure alkali metals (E^0 (M^+/M^0) ≈ −3 V), as reported in the literature cited below.
112. J. Balej, *Electrochim. Acta*, 1976, **21**, 953-956.
113. M. M. Olmstead and P. P. Power, *J. Am. Chem. Soc.*, 1986, **108**, 4235-4236.
114. X. Li, S. Wu, S. Chen, Z. Lai, H.-B. Luo and C. Sheng, *Org. Lett.*, 2018, **20**, 1712-1715.
115. The theoretically expected value of $^1J(^{13}C,^1H)$ = 172.6 Hz for methine (*C3*)H group in **2**, based on the gyromagnetic ratio $\gamma(^2H)/\gamma(^1H)$ = 26.7519/4.1066, was indeed observed as a doublet satellite in the ^1H NMR spectrum.
116. M. Stein, W. Winter and A. Rieker, *Angew. Chem. Int. Ed.*, 1978, **17**, 692-694.
117. S. Grimme and P. R. Schreiner, *Angew. Chem. Int. Ed.*, 2011, **50**, 12639-12642.
118. T. Takeda, Y. Uchimura, H. Kawai, R. Katoono, K. Fujiwara and T. Suzuki, *Chem. Lett.*, 2013, **42**, 954-962.
119. Y. Uchimura, T. Takeda, R. Katoono, K. Fujiwara and T. Suzuki, *Angew. Chem. Int. Ed.*, 2015, **54**, 4010-4013.
120. T. L. Chu, *J. Am. Chem. Soc.*, 1953, **75**, 1730-1732.
121. J. M. Mayer, *Acc. Chem. Res.*, 2011, **44**, 36-46.
122. J. J. Warren, T. A. Tronic and J. M. Mayer, *Chem. Rev.*, 2010, **110**, 6961-7001.
123. B. de Bruin, W. I. Dzik, S. Li and B. B. Wayland, *Chem. Eur. J.*, 2009, **15**, 4312-4320.
124. D. C. Eisenberg, C. J. C. Lawrie, A. E. Moody and J. R. Norton, *J. Am. Chem. Soc.*, 1991, **113**, 4888-4895.
125. H.-S. Dang, V. Diart, B. P. Roberts and D. A. Tocher, *J. Chem. Soc., Perkin Trans. 2*, 1994, DOI: 10.1039/P29940001039, 1039-1045.
126. I. G. Green and B. P. Roberts, *J. Chem. Soc., Perkin Trans. 2*,, 1986, DOI: 10.1039/P29860001597, 1597-1606.

View Article Online
DOI: 10.1039/D6DT01280A

127. J. N. Kirwan and B. P. Roberts, *J. Chem. Soc., Chem. Commun.*, 1988, DOI: 10.1039/C39880000480, 480-482.
128. H. Asakawa, K.-H. Lee, K. Furukawa, Z. Lin and M. Yamashita, *Chem. Eur. J.*, 2015, **21**, 4267-4271.
129. D. Wang, C. Mück-Lichtenfeld and A. Studer, *J. Am. Chem. Soc.*, 2019, **141**, 14126-14130.
130. D. Wang, K. Jana and A. Studer, *Org. Lett.*, 2021, **23**, 5876-5879.
131. S. Shi, F. Salahi, H. B. Vibbert, M. Rahman, S. A. Snyder and J. R. Norton, *Angew. Chem. Int. Ed.*, 2021, **60**, 22678-22682.
132. S.-H. Ueng, A. Solovyev, X. Yuan, S. J. Geib, L. Fensterbank, E. Lacôte, M. Malacria, M. Newcomb, J. C. Walton and D. P. Curran, *J. Am. Chem. Soc.*, 2009, **131**, 11256-11262.
133. J. C. Walton, M. M. Brahmi, L. Fensterbank, E. Lacôte, M. Malacria, Q. Chu, S.-H. Ueng, A. Solovyev and D. P. Curran, *J. Am. Chem. Soc.*, 2010, **132**, 2350-2358.
134. J. C. Walton, *Angew. Chem. Int. Ed.*, 2009, **48**, 1726-1728.
135. M. Mantina, A. C. Chamberlin, R. Valero, C. J. Cramer and D. G. Truhlar, *J. Phys. Chem. A*, 2009, **113**, 5806-5812.

View Article Online
DOI: 10.1039/D6DT01280A

The authors confirm that the data supporting the findings of this study are available within the article and its supplementary materials. The raw data supporting this study are available from the corresponding author upon request, as no institutional data repository is currently available at our university.